

NOT FOR PUBLICATION  
See note overleaf

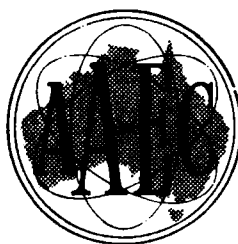
AAEC/PR44-PD  
INDC (AUL) - 28/G



XA04N2778

AAEC/PR44-PD

INDC (AUL) - 28/G



INIS-XA-N--166

# AUSTRALIAN ATOMIC ENERGY COMMISSION

## RESEARCH ESTABLISHMENT

### LUCAS HEIGHTS

PROGRESS REPORT OF PHYSICS DIVISION

1st OCTOBER, 1977 TO 30th SEPTEMBER 1978

ACTIVING DIVISION CHIEF - MR. W. GEMMELL

NOT FOR PUBLICATION

This report was printed for circulation within the Australian Atomic Energy Commission. It has not been reviewed for general use.

It is made available on the understanding that the information it contains will not be quoted in publications, listed in abstracts, journals or communicated to the press.

AUSTRALIAN ATOMIC ENERGY COMMISSION

RESEARCH ESTABLISHMENT

LUCAS HEIGHTS

PROGRESS REPORT OF PHYSICS DIVISION

1st OCTOBER, 1977 TO 30th SEPTEMBER, 1978

ACTING DIVISION CHIEF - MR. W. GEMMELL



# CONTENTS

	Page
1. INTRODUCTION	1
2. REACTOR STUDIES	2
2.1 Moata Operations	2
2.2 Soil Moisture Studies	2
2.3 Fuel Cycle Studies	2
2.3.1 Thorium fuel cycle	2
2.3.2 Uranium-233 and nuclear proliferation	3
2.3.3 Radiation field associated with uranium ore concentrates	3
2.4 Neutron Spectra in Heavy Metal Assemblies	3
2.4.1 Time-dependent spectra in heavy metal assemblies	3
2.4.2 Calculation of time-dependent spectra in heavy metal assemblies	4
2.5 HIFAR Dynamics	5
2.6 Reactor Safety	5
2.6.1 LOCA analysis	5
2.6.2 Reactor transients	10
2.7 Reactor Code Development	10
2.7.1 AUS modular scheme	10
2.7.2 AUS module POW3D	10
2.7.3 Rectangular cell calculations	11
2.7.4 Neutron transport theory - calculation of albedos	12
2.7.5 AAEC shielding handbook	13
3. NEUTRON PHYSICS	13
3.1 Neutron Capture Studies in Collaboration with Oak Ridge National Laboratory	13
3.1.1 Resonance neutron capture in $^{23}\text{Na}$ and $^{27}\text{Al}$ from 3 to 600 keV	13
3.1.2 Neutron capture cross sections in the fission product mass region	13
3.1.3 Neutron capture cross section of $^{57}\text{Fe}$	16
3.1.4 s-wave resonance parameters in the structural materials	16
3.1.5 keV neutron capture in $^{141}\text{Pr}$	16
3.2 Neutron Capture Research Carried Out in Collaboration with Brookhaven National Laboratory	16
3.2.1 Gamma rays from the 5.9 keV resonance in $^{27}\text{Al}$	16
3.2.2 Determination of the spin of the 398 eV resonance in $^{35}\text{Cl}$	17
3.2.3 Capture of 2 and 24 keV neutrons by Mn	17
3.2.4 Capture of 2 and 24 keV neutrons by the Zr isotopes	17
3.2.5 Capture of 2 and 24 keV neutrons by $^{145}\text{Nd}$	17
3.2.6 Capture cross section of Th	17
3.2.7 Symmetry of $^{10}\text{B}(n,\alpha)^7\text{Li}$ yield	17
3.3 Resonance Neutron Capture Spectroscopy in $^{28}\text{Si}$	18
3.4 Neutron Capture Studies at Lucas Heights	19
3.4.1 Neutron capture cross section of $^{170}\text{Yb}$	19
3.4.2 Branching ratio of $^{176}\text{Lu}$ at astrophysical energies	19

# CONTENTS (cont'd)

	Page
3.4.3 Radiative widths of scattering resonances	21
3.4.4 Neutron capture mechanisms in the 3s size resonance	21
3.4.5 Non-statistical neutron capture mechanisms in $^{139}\text{La}$ and $^{141}\text{Pr}$	23
3.5 Fission Studies	25
3.5.1 $^{252}\text{Cf}$ spontaneous fission neutron spectrum	25
3.5.2 Neutron detector efficiency	29
3.5.3 Fission barrier for the thorium isotopes	30
3.5.4 Measurement of kinetic energies of $^{239}\text{Pu}$ , $^{235}\text{U}$ fission fragments in the resonance region	30
3.5.5 Preparation of $^{239}\text{Pu}$ targets by electrospraying	34
4. NUCLEAR TECHNIQUES	36
4.1 3 MeV Van de Graaff Accelerator	36
4.2 Data Acquisition Facilities	39
4.2.1 Bibliography	40
4.3 Ion Scattering and Implantation	40
4.3.1 Ion scattering techniques	40
4.3.2 H and He implantation	40
4.4 Proton Decoration of Fluorite	41
4.5 Proton Induced X-rays	41
4.5.1 Thorium and uranium analysis	43
4.6 Moata Applications	44
4.6.1 Uranium analysis	44
4.6.2 Neutron radiography	44
4.6.3 Thorium analysis	48
4.6.4 Particle track analysis	48
4.7 Bore Hole Logging	48
5. RUM JUNGLE ENVIRONMENTAL STUDIES	49
5.1 Determination of Ground Water in White's Overburden Dump	49
5.2 Temperature Profiles within White's Dump	49
5.3 Computer Simulation of Water Flows	51
6. FUSION	53
6.1 Australian National University	53
6.1.1 Soft X-ray measurements on LT-4	53
6.2 Flinders University of South Australia	53
6.3 Sydney University	55
6.3.1 Plasma heating due to magnetic field reversal	55
6.3.2 Tearing mode instabilities	55
6.4 Plasma Equilibrium Calculations	55
6.4.1 Fusion data library	56
6.4.2 Atomic and molecular data needs for fusion reactors	56
7. MISCELLANEOUS	56
7.1 Magnetohydrodynamic Turbine	56
7.2 Application of Unfolding Techniques	56
7.2.1 Measured resolution functions	56

# CONTENTS (cont'd)

	Page
7.2.2 Activation methods to determine neutron flux	57
7.2.3 Flux spectrum unfolding for HIFAR	57
7.3 Neutron Therapy	57
7.4 Deep Ocean Currents and Disposal of Radioactive Waste into the Ocean	58
7.5 Inverse Reaction Problem	58
7.6 Pressure Dependence of Plasma Formation under Laser Radiation	58
8. PUBLICATIONS	59
8.1 Papers	59
8.2 Reports	50
8.3 Conference Papers	61
Physics Division Seminars	63
Table 2.1 Comparison of cell models for AAEC $^{235}\text{U/C}$ assembly - 7-group calculations	
Table 3.1 30 keV Maxwellian averaged radiative capture cross sections from the present data	
Table 3.2 Table of average resonance parameters	
Table 3.3 Comparison of groundstate and total radiative widths	
Table 3.4 Partition of s-wave radiative widths in the 3s region	
Table 4.1 Accelerator time allocation	
Table 4.2 Comparison of theoretical and experimental $\text{La X-ray}$ yields	
Fig. 2.1 Pressure in the discharge nozzle of a large vessel during LOCA	
Fig. 2.2 Vessel and choke pressures during LOCA	
Fig. 3.1 Neutron time of flight spectra for $\text{Yb}_2\text{O}_3$	
Fig. 3.3 Time of flight neutron spectra at different bias settings	
Fig. 3.4 $^{252}\text{Cf}$ spontaneous fission neutron spectrum	
Fig. 3.5 Deviation of $^{252}\text{Cf}$ spontaneous fission spectrum from Maxwellian distributions (6 to 14 MeV)	
Fig. 3.6 Absolute efficiency of neutron detector from 2 to 10 MeV	
Fig. 3.7 $^{239}\text{Pu}(n,f)$ : single detector fission fragment pulse height distribution	
Fig. 3.8 $^{239}\text{Pu}(n,f)$ : total pulse height distribution (summed from two complementary detectors)	
Fig. 3.9 Apparatus for electrospraying of $^{239}\text{Pu}$	
Fig. 4.1 Proton irradiation of fluorite	
Fig. 4.2 Typical PIXE spectra	
Fig. 4.3 Uranium concentration as a function of induced X-ray activity	
Fig. 4.4 Thorium concentration as a function of induced X-ray activity	
Fig. 5.1 Variation of count rate about centre line of drums filled with sand/polythene mixtures	
Fig. 5.2 Variation about mean of temperatures within White's overburden dump	





## 1. INTRODUCTION

Two main features influenced the year's activities: the Government's constraints on staffing and the Commission's views on research and development objectives. The reduction in staff numbers in Physics Division was by natural wastage, chiefly in the technical officer area. This has reduced operation of the reactor to a major extent and of the accelerator, both of which are now somewhat under-staffed and inadequately serviced.

The second influence was the view of the Commission that research activities should move away from the more traditional areas of nuclear energy towards problems of the front end of the fuel cycle and the environment. Also, the Commission decided to place increasing emphasis on fusion and possibly on alternative energy studies.

Neutron capture studies were continued, mainly in collaboration with Oak Ridge National Laboratory, Brookhaven National Laboratory and Bruyères-le-Châtel and, to a lesser extent, the Australian universities, with the objective of improving our understanding of the capture mechanism and of seeking applications of the results and techniques developed in the neutron capture research. Results from the measurement of the  $^{252}\text{Cf}$  spontaneous fission neutron spectrum are now available in reasonably final form. Other fission work was concerned with the shape of the fission barriers for the thorium isotopes and with confirming  $\bar{\nu}$  differences between the  $0^+$  and  $1^+$  resonances of  $^{239}\text{Pu}$ .

Commercial acceptance of the delayed neutron method of analysing ore samples for uranium continued to gain ground. There was interest in the possibility of a similar service for thorium and the advantages of nuclear techniques of analysis became more widespread. Several of these techniques (backscattering, proton induced X-ray emission (PIXE), fission track) were actively developed. The major restraint was unavailability of staff. Particularly interesting was the colouration produced by proton irradiation of natural fluorite crystals. This colouration highlighted dislocations, growth patterns and surface features.

The main thrust of the nuclear energy work was the numerical analysis of reactors and loss of coolant accidents, in particular the numerical methods used in the solution of partial differential equations. We were encouraged with the results obtained in analysing the CSNI standard problems. Several interesting areas and topics were revealed for further work.

Although our study of SPERT type transients led to satisfactory agreement with experiment, the physical mechanism causing the high transient heat transfer still eludes us.

Interesting information was obtained on the temperatures existing in the Rum Jungle overburden heaps. If real, they are inconsistent with the conventional view of bacterial activity. Remeasurement will be carried out in some detail in the forthcoming wet season (November-March).

Several staff members were seconded to three universities to assist in plasma physics research.

## 2. REACTOR STUDIES

### 2.1 Moata Operations

The reactor operated for 420 hours with a total energy production of 21.5 MWh. The main use was for uranium ore analysis and neutron radiography. Research studies carried out during the year included:

- A joint collaborative program with the Research School of Biological Science, Australian National University, to investigate the accumulation and distribution of uranium in brain tissue, with a view to investigating behaviour effects in animals.
- An investigation into the accumulation of uranium in hair.
- Fission track analysis of the distribution of fissionable and fertile materials in biological specimens.
- Investigation of the metabolic pathways of Pu species by fission track analysis of biological specimens.
- Measurement of the neutron absorption cross section of soils to provide data for bore hole calculations.
- Some aspects of neutron radiation on cells in vivo (Department of Biochemistry, University of Queensland).
- Determination of the rate of growth in plant roots in differing soil conditions by neutron radiography (Department of Agriculture, University of La Trobe).

The linear control ion chamber was replaced during January-February and the opportunity was taken to renew radiation damaged electrical cables, to equip the start-up channel with triaxial cables in an attempt to reduce the start-up trips caused by interference and to flatten the absorber plates on the control rods.

### 2.2 Soil Moisture Studies

Calculations were made on the neutron scattering properties of soil under conditions of changing density, absorption cross section and water content of the soil. The thermal flux arising from the neutron equivalent of a Pu/Be source was calculated at a detector position close to the source, placed in an infinite soil and water complex for the varying soil conditions. Small, high neutron leakage systems (44 gallon drums) are frequently used experimentally to standardise bore hole equipment. Monte Carlo methods are being used to study such localised effects as the perturbations due to a highly absorbing lithium glass detector and a Pu/Be source, which often arise in calculating small, high leakage situations.

### 2.3 Fuel Cycle Studies

#### 2.3.1 Thorium fuel cycle

A review of the thorium fuel cycle was made and compared with other fuel cycles. The suitability of various types of reactor to the thorium fuel cycle and the probable effects on the fission energy resources were analysed. Some systems showed considerable promise when operated on the thorium cycle, both in economic

and in resource conservation terms. No real disadvantage appeared when compared with the uranium cycle, but considerable development effort and engineering scale demonstration are required.

### 2.3.2 Uranium-233 and nuclear proliferation (B. E. Clancy)

As background material for INFCE studies, a review was prepared of those properties of the three fissile materials,  $^{233}\text{U}$ ,  $^{235}\text{U}$  and  $^{239}\text{Pu}$ , which would be important both to nationally supported and to clandestine construction of nuclear weapons. Properties reviewed included prompt critical masses, neutron lifetimes, the number of prompt fission neutrons released per fission event and neutron source strengths arising from spontaneous fission and from  $(\alpha, n)$  reaction in light nuclei associated with the fissile materials. Gamma ray doses arising from the radioactive daughters of  $^{232}\text{U}$  were calculated from a number of assumptions about the mode of production of  $^{233}\text{U}$  from thorium. There have been references in supposedly prestigious scientific journals to the belief that  $^{233}\text{U}$  is a most desirable fissile material because the associated  $^{232}\text{U}$  activity will automatically safeguard the fissile isotope.\* The review indicates that  $^{233}\text{U}$  will need as much safeguarding as the other fissile materials.

### 2.3.3 Radiation field associated with uranium ore concentrates (B. E. Clancy)

Substantial quantities of  $\text{U}_3\text{O}_8$  concentrates are held in the stockpile at Lucas Heights. The quantity and concentration of the oxide is such that the natural radioactive decay gives rise to a significant source of  $\gamma$ -rays - the most important component associated with the  $\beta$ -decay to  $^{234}\text{U}$ . The high density of the oxide fortunately means that self-shielding by the oxide is very effective. Calculations have been made of dose rates in air at a number of positions in the radiation field and for a number of source configurations. The aim is to provide simple recipes for predicting dose rates to operators who must enter the field as the stockpile is depleted or replenished. A complication arises from the presence of thorium concentrates in the storage area.

## 2.4 Neutron Spectra in Heavy Metal Assemblies

### 2.4.1 Time dependent spectra in heavy metal assemblies (S. Whittlestone)

The experimental work for the determination of time-dependent neutron energy spectra was completed for a depleted uranium stack with source neutrons in the range 0.5 to 6 MeV. The small NE213 liquid scintillator probe used acted as a time-gated neutron spectrometer. The neutron energy spectra was unfolded from pulse height distributions of the recoil protons.

Extensive calibrations of the detector system included measurements of efficiency, the monoenergetic neutron responses, timing walk of the discriminator and the effect of count rate on neutron-gamma discrimination. The first of these, the efficiency, was measured by comparing the time of flight spectra taken simultaneously by the scintillator probe and by a larger scintillator whose efficiency was known. Time of flight spectra were also used to determine the monoenergetic neutron responses, but

---

\*Davies, J. (1977) - Conserving uranium without the fast breeder. Nature, Vol. 270 1/12/77.

corrections for poor energy resolution were necessary at high energies. These responses were fitted to a sum of two exponentials, plus a resolution broadened step function and the parameters adjusted requiring that they vary smoothly with energy and that the resolution should not worsen with energy. Some measurements were made with a monoenergetic neutron beam defined by the associated triton from the  $D(d,n)T$  reaction. While these measurements suffered from poor statistics, they were most valuable in giving confidence to the response parameter adjustments. The monoenergetic neutron profile set to be used in spectrum analysis was generated from these adjusted parameters.

The third calibration required was the measurement of walk - the change in timing of the scintillator discriminator as a function of pulse height. The values of walk in units of time channel widths were fed into the PDP-15 program, DIGWIN-W, which then sorted events into the appropriate time channel according to their pulse height. Walk was measured using a pulsed deuteron beam on a lithium target and placing the detector as close to the target as possible, thereby avoiding time of flight time dispersion of the beam. The variation of the mean of the time spectra taken from digital windows in the pulse height spectra was used as a measure of the walk.

The final calibration of the detector system, the effect of count rates on neutron  $\gamma$ -ray discrimination, was measured using a  $\gamma$  source placed at different distances from the detector to obtain a range of count rates with the same spectrum. Even though a test pulse was unchanged in height, the pulse shape was affected by high count rates and the  $\gamma$ -ray rejection deteriorated from 99.9% to 98% for  $^{137}\text{Cs}$   $\gamma$ -rays when the count rate increased from 700 to 3000 Hz. Using this data and measuring the dependent  $\gamma$ -ray spectra in the uranium stack, it was possible to estimate the proportion of counts in the neutron spectra which could be attributed to  $\gamma$ -rays. For most of the data, the  $\gamma$ -ray contamination was less than the errors from other causes (a few per cent).

The actual time dependent spectrum measurement was made during a period of one hundred hours when all the equipment worked consistently well. Spectra were taken over the range 1 to 77 ns in 17 time windows selected to optimise count rate without losing too much timing information.

Analysis of the data is approaching completion. All the peripheral data handling coding are complete and the main unfolding code is in its final stages of development.

#### 2.4.2 Calculation of time dependent spectra in heavy metal assemblies (M. T. Rainbow)

An NE213 organic liquid scintillator was used by Whittlestone to measure proton recoil spectra as a function of time in the pulsed depleted uranium assembly, using a 2.4 MeV thick target  $^9\text{Be}(d,n)^{10}\text{B}$  source. These proton recoil spectra are being unfolded to yield time-dependent spectra of the neutron flux integrated over a set of time windows. The MORSE Monte Carlo transport code was used to calculate this experiment.

The MORSE calculations were performed with a source pulse profile, having a

narrow (short duration, 0.1 ns) rectangular form. Time-dependent spectra suitable for comparison with experiment were synthesised by convoluting the raw MORSE results with a histogram representation of the experimental source pulse profile (FWHM  $\sim 3$  ns). Routines were written to perform this folding, to integrate the resulting spectra over the experimental time windows and to perform the associated error analysis. These results will be compared with experiment when the analysis of the experimental results is completed.

## 2.5 HIFAR Dynamics (J. R. Harries)

An apparent decrease in the reactivity worth of the HIFAR coarse control arms (CCAs) highlighted the need for a better method of reactivity calibration. The inverse kinetics procedure developed for the investigation into temperature and flow transients was adapted for use in calibrating the CCAs. The inverse kinetics method includes the contribution of the photoneutron source, which causes difficulties in the asymptotic doubling time method previously used.

The new procedures were used to recalibrate the CCAs and a series of experiments were carried out with different core masses to determine the dependence of the CCA worth on the core mass. The reactivity worth was found to be  $M^{-0.75 \pm 0.10}$  where  $M$  is the mass of fissile material in the core. The apparent decrease in the reactivity worth was caused by the correction for the mass dependence of the CCA worth and the temperature coefficient.

A computer program has been written which will enable the inverse kinetics procedure to be used as the standard method for the periodic calibrating of the CCAs.

## 2.6 Reactor Safety

### 2.6.1 LOCA analysis (W. J. Turner, G. D. Trimble)

#### NAIAD Development

One of the problems which can arise in the simulation of a loss of coolant accident in a nuclear reactor is the presence of supersonic flow. The finite difference scheme used in NAIAD is numerically unstable for supersonic flow. A new difference scheme, almost identical to the old scheme for subsonic flow, was developed which is stable for supersonic flow. In essence, upwind differencing is applied to all three conservation equations in the presence of supersonic flow. The method gave reasonable results for a converging-diverging nozzle in which the downstream boundary pressure is slowly reduced. The flow accelerates until choked flow occurs; then a compression shock forms and slowly moves through the diverging section until only supersonic flow is present downstream of the choke point. As expected, the choke point was slightly downstream of the minimum area. Unfortunately, the method does not allow a supersonic-to-subsonic transition to occur in response to a change in the downstream boundary condition, and hence has not been incorporated in the standard NAIAD code. However, the supersonic code is being used at Oak Ridge National Laboratory for air, He and  $\text{UF}_6$  flows, in which only the subsonic-to-supersonic transition occurs.

### Thermodynamic Nonequilibrium

The simplest way to include thermodynamic nonequilibrium in a hydraulic simulation is to use the drift flux model (Zuber 1967)<sup>1</sup>. A computer code has been written which simulates the hydraulic behaviour of a variable area flow channel by solving the one-dimensional time-dependent drift flux equations. These equations comprise the usual conservation of mass, momentum and energy of the two phase mixture, plus an equation for the conservation of the vapour mass. A vapour source term describes the rate of creation or destruction of vapour. The form of the vapour source term has been taken from Rivard et al. (1975)<sup>2</sup>. The vapour is assumed to be always saturated and that the vapour source is proportional to the departure of the liquid temperature from saturation. Large values of the proportionality constant force the system to stay near thermodynamic equilibrium, while a zero value produces 'frozen quality' flow in which no vapour source is present. An odd fact about the four equation drift flux model is that the choke flow rate for a given set of local conditions is independent of this proportionality constant. It is, in fact, the 'frozen quality' choke flow rate. Numerical experiments were carried out on a converging-diverging nozzle to investigate this difference between the four equation drift flux model and the three equation thermodynamic equilibrium model. For fixed inlet conditions, the maximum flow rate through the nozzle was the same for the three equation model and for the four equation model, using a large value of the proportionality constant. This is in spite of the fact that the choking planes are at different locations and at different pressures in the two models.

### OECD-NEA LOCA Standard Problems

Australian participation in the OECD-NEA/CSNI Working Party on Emergency Core Cooling continued with further work being done on standard problems.

The final CSNI report on standard problem 6 (blowdown of a large pressure vessel through a small pipe at two-thirds height) has been issued (Winkler 1978)<sup>3</sup>. In order to simulate this experiment it was found necessary to extend the NAIAD code by including a vessel model, which is based on the bubble rise model (Moore and Rose 1966)<sup>4</sup>, but allows for a saturated steam dome over subcooled water. Figure 2.1 shows the results obtained with NAIAD and the other thermodynamic equilibrium codes. It is notable that three of the simulations exhibit non-physical oscillation which appear to indicate numerical instabilities.

Further work has been done on standard problem 3 in which some difficulties were experienced in earlier calculations during the flow reversal. These were traced to discontinuities in the heat flux as a function of quality. The heat transfer package has been amended so that the heat flux is a smooth function of flow, pressure, enthalpy and wall temperature, except at the onset of dryout.

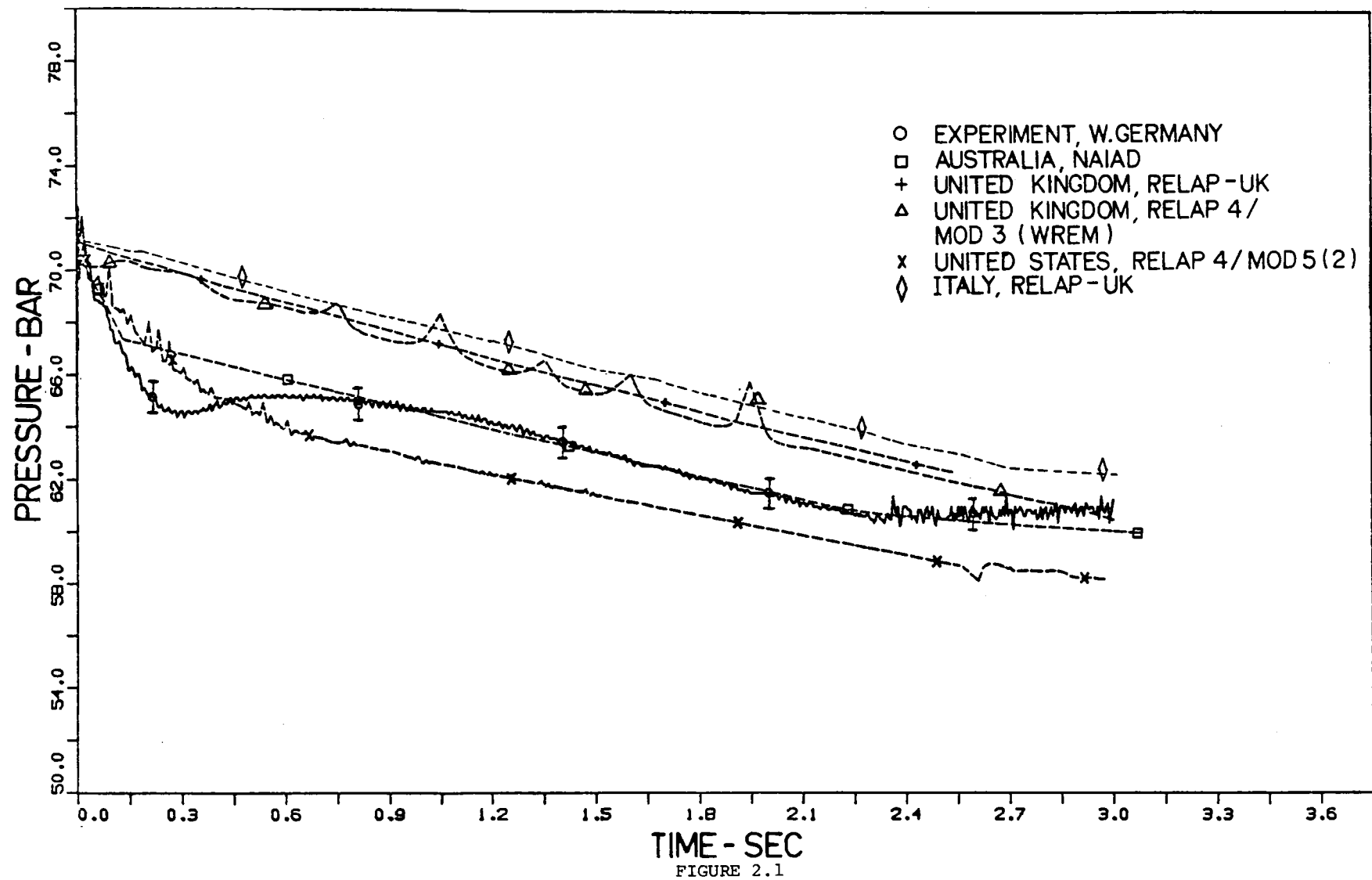
---

<sup>1</sup>Zuber, N. (1967) - Flow excursions and oscillations in boiling two-phase flow systems with heat addition. Symp. Two-Phase Flow Dynamics. EUR-4288e, 1071.

<sup>2</sup>Rivard, W. C., Travis, J. R. and Tarrey, M. D. (1975) - Numerical calculation of two-phase flow in a shock tube. LA-UR-76-917.

<sup>3</sup>Winkler, W. (1978) - Comparison report on OECD-CSNI standard problem No. 6. CSNI Report No. 30.

<sup>4</sup>Moore, K. V. and Rose, R. P. (1966) - Application of a lumped parameter bubble-rise model to coolant blowdown analysis. Trans. Am. Nucl. Soc. 9, 2, 559.



PRESSURE IN THE DISCHARGE NOZZLE OF A LARGE VESSEL DURING LOCA

### Presentation of Computer Output

(with A. W. Dalton and J. W. Fredericks)

A problem posed by large computer code calculations is the comprehension of the results obtained. This is particularly true in LOCA simulation where the result is usually some half a million numbers comprising flow, pressure, enthalpy, density, wall temperature, etc., at each node at each time step. The presentation on a CRT screen of, say, pressure versus position at time zero, followed by the same graph for successive time steps, has proved to be an extremely valuable adjunct for analysis. The high speed DATAWAY link allows this to be done at about six frames per second, i.e. as a motion picture. The movement of pressure waves and the general result of the calculation is comprehended in a relatively short time.

A photographic system to record this motion picture on film was set up with the operation of a time lapse camera controlled from the computer software. A motion picture was made of the standard problem 3 simulation for presentation at the Third Meeting of the Australian Simulation Society, Canberra, September 4-6, 1978. It is hoped to make this facility available to all computer users.

### Modelling of the AAEC Blowdown Experiments

(A. W. Dalton, G. D. Trimble)

The modelling of the Engineering Division's blowdown experiments has been concluded. A more realistic representation of two-phase flow in the vertical pressure vessel was achieved using the vessel model developed for standard problem 6. Calculations using the model were successful in reproducing not only the magnitude of the choking pressure during the transient, but also the two distinct stages observed in its variation during the transient. However, the time at which the knee occurred in the NAIAD curve exceeded the experimental value by a factor of 1.2 in the three different experiments reported (Figure 2.2). The best agreement was obtained using the slip model of Beattie (1974)\*.

### Reactor Kinetics

A reactor kinetics model is being developed using the point kinetics model from ZAPP. Reactivity feedback is calculated from temperatures and densities calculated in NAIAD.

### New Research Reactor

(J. W. Connolly, A. W. Dalton)

Preparatory work is underway to assemble the basic knowledge required for safety studies for the new research reactor in the fields of containment, fission product plumes, flow transients and reactivity transients.

---

\*Beattie, D. H. R. (1974) - AAEC private communication



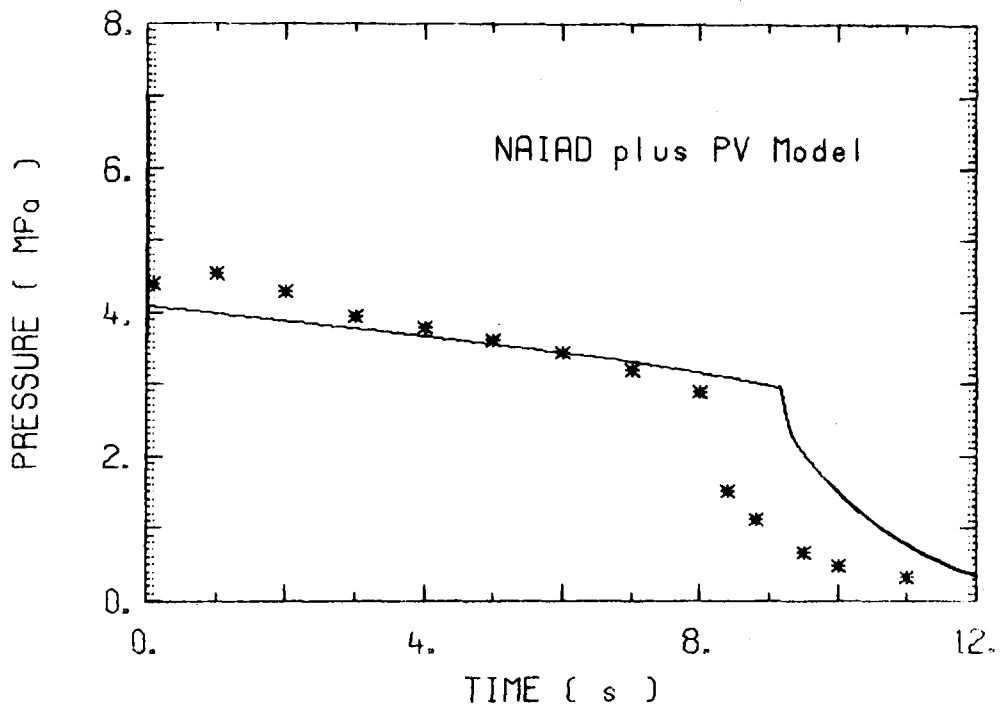
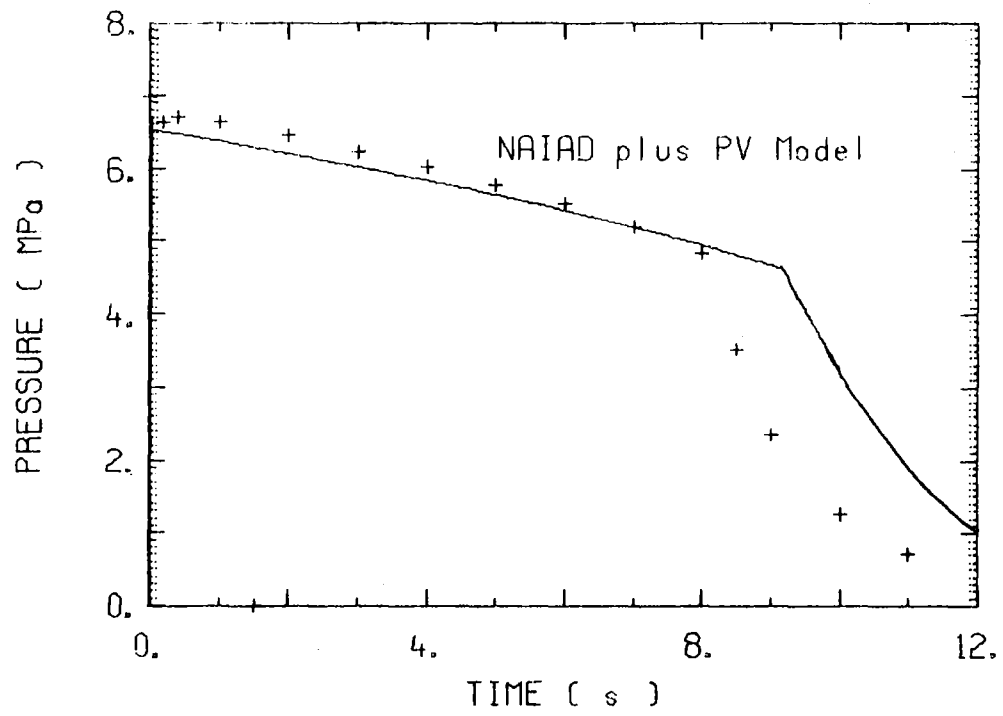


Figure 2.2 Vessel and choke pressures during LOCA

### 2.6.2 Reactor transients (J. W. Connolly)

Attempts to formulate a physical basis for the high conduction transient boiling model have not met with success, although numerical calculations gave qualitative insight into the way in which temperature distributions, established prior to boiling, collapse after initiation of the high heat transfer phase of boiling.

The central problem is lack of identification of a process to produce the high heat transfer apart from bubble formation. The SPERT analyses of cores with widely different void coefficients suggests very strongly that bubble void development is not an important mechanism in producing high heat transfer from fuel plate to coolant and the heat transfer model used in these calculations provided a very satisfactory coupling between the power period and the boiling heat transfer rate. This model also satisfactorily describes transient boiling phenomena from these platinum ribbons; however, photographic evidence from these experiments shows rapid bubble development in phase with the high heat transfer. To allow this in the SPERT analysis would destroy the good agreement between calculation and experiment already established.

Further calculations have been performed to establish consequences of reactivity transients in HIFAR. It appears that the maximum tolerable excursion would result in almost complete expulsion of the reactor coolant over a time of ~80 ms and that possible fuel element distortion must not prevent the control arms from entering the core. This is receiving further attention.

### 2.7 Reactor Code Development

#### 2.7.1 AUS modular scheme (J. Barry\*, B. Harrington, J. Pollard, G. Robinson)

Work for the period mainly centred around commissioning the 3D diffusion model POW3D along with the necessary edit routines. A revision of the basic cross section library group structure is underway in preparation for the next ENDF/B library release.

#### 2.7.2 AUS module POW3D (J. Barry, B. Harrington, J. Pollard)

POW3D is a 3D diffusion theory 'workhorse' module based on a finite difference approximation to the group diffusion equation in (n,y,z) geometry. For 2D or 1D, other geometries are available as POW3D is to essentially replace the present POW module. Present experience with POW3D for steady state calculations shows an improvement over POW for 2D calculations. This is mainly because POW3D is normally run using the method of implicit non-stationary iteration, MINI, to solve the flux equations, although greater care in calculating source terms also reduces the machine time.

At the present time, the following solution options are available:

1. For (x,y) plane inners: SLOR, MINI or ICCG.
2. For between plane (z) inners: SLOR, MINI or ICCG (if also used for (1)).
3. For group solution: GS or MINI, where SLOR stands for the successive line over-relaxation approach; ICCG stands for the incomplete Choleski conjugate gradient method, and GS stands for the Gauss-Seidel method.

---

\* Applied Mathematics and Computing Division

Experience to date suggests that the best solution option is MINI for everything, although ICCG is only in the early stages of testing. Certainly when using MINI for solution of the group equations, where normally the GS method would be used, the time saving for some problems involving intensive upscatter has been a factor of 2. Since fission is treated in kinetics calculations as part of the 'scatter' matrix, this large time saving will greatly benefit such calculations when kinetics aspects are implemented in POW3D.

### 2.7.3 Rectangular cell calculations (G. Robinson)

The accuracy of the simple one-dimensional slab models usually adopted to represent the rectangular cell geometry often occurring in experimental assemblies has been checked for a recent AAEC  $^{235}\text{U}$ /graphite assembly. Two-dimensional cell calculations against which the one-dimensional models could be compared, were performed with a modified version of the DOT-3.5 code. The thin fuel strips (0.58 mm) require a high order angular quadrature to represent flux peaking in the fuel strip at high energies. The quadrature set used was a  $DP_{n/2-1}(\eta)T_n(\mu)$  set of Lathrop and Carlson (1964)<sup>1</sup>, where  $\eta$  is the cosine with respect to the normal to the fuel slab. Sixteen  $\eta$  levels per octant were used, but the number of  $\mu$  points per  $\eta$  level varied from 1 to 4 only.

The modifications to DOT included the removal of a number of coding errors particular to this case, improving the convergence by including the boundary conditions in the inner iteration scaling, improving the neutron balance obtained and adding AUS output options. It was found that convergence with reflected boundary conditions was very slow and did not occur at all for some cases. In particular, one-dimensional simulations in DOT converged only for an infinite mesh interval in the unrepresented direction.

The results of the cell model comparison are given in the Table 2.1. The one-dimensional models are:

- 1D(a) - maintains fuel density and thickness while adjusting the moderator thickness to give the correct volume ratio.
- 1D(b) - conventional volume smearing in the transverse direction which gives a relative fuel density of 0.508.
- 1D(c) - a mixture of 1D(a) and 1D(b) which gives the correct material buckling by using a relative fuel density of 0.945.

It can be seen that the 1D(a) model, which has been extensively used at the Research Establishment, gives quite fair results, while the 1D(b) model does not. The point of setting up a model such as 1D(c) is that having established the model in a few group calculation, it may be used in multigroup calculations.

---

<sup>1</sup>Lathrop, K. D. and Carlson, B. G. (1964) - Discrete ordinate angular quadrature of the nucleon transport equation. LA-3186.

TABLE 2.1  
COMPARISON OF CELL MODELS FOR AAEC  $^{235}\text{U}/\text{C}$  ASSEMBLY -  
7-GROUP CALCULATIONS

		2-Dimensional	1D(a)	1D(b)	1D(c)
			% Error		
Group Flux Ratio	$k_{\infty}$	1.7673	+0.08	-0.35	+0.03
Fuel/Moderator	$B_m \text{ cm}^{-1}$	$2.290 \times 10^{-3}$	-0.25	+1.60	0.0
1.	2.9 MeV	1.991	+3.9	-26	+0.5
2.	2.9 MeV - 0.82 MeV	1.433	+3.7	-16	+1.5
3.	0.82 MeV - 41 keV	1.099	+1.7	-4.6	+0.9
4.	41 keV - 2 eV	0.922	-0.9	+4.3	-0.3
5.	2 eV - 0.6 eV	0.842	-1.6	+9.2	-0.4
6.	0.6 eV - 0.1 eV	0.633	-2.9	+26	0.0
7.	0.1 eV - 0.0 eV	0.441	-2.6	+50	+2.2

#### 2.7.4 Neutron transport theory - calculation of albedos

The calculation of neutron transport through ducts and other penetrations in bulk media is a longstanding problem in shielding theory. Unless handbook recipes are to be used, recourse is usually made to Monte Carlo methods for the calculations. At the end of the duct, remote from any sources, neutron fluxes are essentially produced by neutrons which have travelled down the different legs of the duct being 'reflected' several times from the walls. For a neutron striking a wall, the probability of its reflection is defined by an albedo, which depends on the angle of incidence and reflection of the neutron and on the incoming and outgoing energies.

A standard method for calculation of the albedos is to use a plane geometry transport code with neutrons impinging on a slab of finite but large thickness and to extract the albedos from the energy angular fluxes calculated by the code. For 'reflection' where the emerging neutron energy is significantly different from the incoming energy, there is little correlation of the energy direction with the incoming direction and many albedo treatments ignore the correlation.

When the neutron emerges (is 'reflected') with an energy little different from the incoming energy (i.e. emerges in the same energy group for multigroup calculations), the incoming and emerging neutron directions are strongly correlated if the within-group scattering is anisotropic.

The angular neutron flux emerging from the wall of a duct is related to that impinging on the wall by the equation

$$\phi(\Omega) = \frac{1}{2\mu} \iint_{\Omega' \cdot \underline{n} < 0} S(\underline{\Omega}, \underline{\Omega}') \phi(\underline{\Omega}') d\Omega' \quad , \quad \underline{\Omega} \cdot \underline{n} > 0$$

where  $\underline{n}$  is a unit vector normal to the surface of the duct and directed outwards from the wall, and  $\mu = \underline{\Omega} \cdot \underline{n}$ . In a Monte Carlo simulation, no tracking of particles in the

interior of the material surrounding the duct is required if the reflection function  $S(\Omega, \Omega')$  is known explicitly.

A technique for direct evaluation of  $S(\Omega, \Omega')$  has been developed and its application to realistic shielding problems is being studied. If the scattering anisotropy is represented by the usual Legendre polynomial, expansion in the scattering angle, a large number (typically greater than ten) of terms must be retained before a satisfactorily smooth representation of the reflection function can be obtained. The study will be continued using representations of the scattering anisotropy other than the classical Legendre expansion.

#### 2.7.5 AAEC shielding handbook (I. J. Donnelly, B. J. McGregor)

The handbook is intended to provide a brief description of both the cross section data libraries and the transport codes which are currently available for shielding calculations at Lucas Heights, and to summarise our experience with them. It is hoped that the information given will be of assistance in the choice of the appropriate cross section data and transport code for a given shielding calculation and in the accurate use of the chosen technique.

The handbook is divided into sections. Part A contains an introduction to the linear transport equation and the methods that are commonly used to solve it in the shielding content. Part B presents some transport and shielding codes available at the AAEC with information regarding their running on the AAEC computer system. (Codes treated are SABINE, ANISN, DOT and MORSE). Part C deals with various available cross section libraries. Part D describes some calculations that have been performed and gives experiences with the use of each code. Work on the preparation of the handbook is nearing completion.

### 3. NEUTRON PHYSICS

#### 3.1 Neutron Capture Studies in Collaboration with Oak Ridge National Laboratory

##### 3.1.1 Resonance neutron capture in $^{23}\text{Na}$ and $^{27}\text{Al}$ from 3 to 600 keV

(A. R. de L. Musgrove, B. J. Allen, R. L. Macklin\*)

The radiative capture cross sections of  $^{23}\text{Na}$  and  $^{27}\text{Al}$  have been measured at Oak Ridge Electron Linear Accelerator (ORELA) and resonance parameters obtained for resonances up to 600 keV. Particular care was taken to correct the data for prompt neutron scattering effects by Monte Carlo methods.

##### 3.1.2 Neutron capture cross sections in the fission product mass region

(A. R. de L. Musgrove, B. J. Allen, J. W. Boldeman, R. L. Macklin)

The radiative capture cross sections for the separated isotopes of Sr, Y, Zr, Mo, Pd, Cd, Ba, La, Ce, Pr and Nd in the range 3 to 200 keV were measured with high resolution at the 40 m station of ORELA. Maxwellian averaged 30 keV cross sections and average resonance parameters derived from the analysis are given in Tables 3.1 and 3.2. A strong dependence of the average radiative widths on neutron binding energy is noted. This leads to a pronounced even-odd disparity. Neutron strength functions reduce with decreasing binding energy along an isotopic chain owing to the decreasing density of doorway states at the binding energy.

---

\*Oak Ridge National Laboratory, Oak Ridge, Tenn. 37830, U.S.A.

TABLE 3.1  
30 keV MAXWELLIAN AVERAGED RADIATIVE CAPTURE  
CROSS SECTIONS FROM THE PRESENT DATA

Nucleus	$\frac{\langle\sigma \cdot v\rangle}{v_T}$	Nucleus	$\frac{\langle\sigma \cdot v\rangle}{v_T}$
$^{86}\text{Sr}$	70±8	$^{110}\text{Cd}$	240±30
$^{87}\text{Sr}$	74±10	$^{111}\text{Cd}$	880±125
$^{88}\text{Sr}$	5.8±0.5	$^{112}\text{Cd}$	220±30
$^{89}\text{Y}$	20.0±3.0	$^{113}\text{Cd}$	715±80
$^{90}\text{Zr}$	17.0±1.0	$^{114}\text{Cd}$	147±25
$^{91}\text{Zr}$	60±8	$^{134}\text{Ba}$	225±35
$^{92}\text{Zr}$	51±6	$^{135}\text{Ba}$	465±80
$^{94}\text{Zr}$	34±5	$^{136}\text{Ba}$	70±10
$^{95}\text{Mo}$	380±50	$^{137}\text{Ba}$	58±10
$^{96}\text{Mo}$	172±25	$^{138}\text{Ba}$	3.9±0.8
$^{97}\text{Mo}$	390±50	$^{139}\text{La}$	36±5
$^{98}\text{Mo}$	100±15	$^{140}\text{Ce}$	7.7±1.0
$^{104}\text{Pd}$	580±60	$^{141}\text{Pr}$	111±15
$^{105}\text{Pd}$	1100±120	$^{142}\text{Nd}$	57±7
$^{106}\text{Pd}$	335±35	$^{143}\text{Nd}$	265±50
$^{108}\text{Pd}$	325±35	$^{144}\text{Nd}$	65±10
$^{110}\text{Pd}$	275±30	$^{145}\text{Nd}$	400±90
		$^{146}\text{Nd}$	115±25

TABLE 3.2  
TABLE OF AVERAGE RESONANCE PARAMETERS

Nucleus	$\langle D \rangle_s$ (eV)	$10^4 S_0$	$10^4 S_1$	$\langle \Gamma \rangle_{\gamma s}$ (meV)	$\langle \Gamma \rangle_{\gamma p}$ (meV)
$^{86}\text{Sr}^*$	3000±1000	0.74±0.34	3.5 ±1.0	240±50	(220)
$^{87}\text{Sr}^*$	(270)	0.30±0.08	4.0 ±1.3	(80)	(125)
$^{88}\text{Sr}^*$	40 000	0.32±0.18	3.1 ±1.5	220±50	390±90
$^{89}\text{Y}$	2200±700	0.32±0.11	4.4 ±1.5	115±15	(210)
$^{90}\text{Zr}^*$	8600±1600	0.54±0.14	4.2 ±0.9	130±20	250±50
$^{91}\text{Zr}$	640±120	0.42±0.12	5.7 ±1.0	140±8	220±12
$^{92}\text{Zr}^*$	3100±1000	0.76±0.28	8.3 ±1.4	135±25	220±50
$^{94}\text{Zr}^*$	3800±1000	0.55±0.16	9.6 ±2.2	85±20	148±28
$^{92}\text{Mo}$	2400±650	0.65±0.25	3.7 ±0.7	160±20	290±35
$^{94}\text{Mo}$	1150±350	0.45±0.25	7.5 ±2.5	135±20	175±30
$^{95}\text{Mo}$	80±25	0.48±0.10	7.5 ±2.5	150±20	
$^{96}\text{Mo}$	950±220	0.54±0.20	8.0 ±2.5	114±14	136±18
$^{97}\text{Mo}$	42±15	0.37±0.15	3.5 ±2.0	130±20	
$^{98}\text{Mo}$	950±150	0.44±0.12	3.3 ±0.7	93±11	117±15
$^{100}\text{Mo}$	420±100	0.51±0.18	3.5 ±1.0	85±11	85±11
$^{106}\text{Cd}$	135±35	1.0 ±0.35	5.0 ±1.5	155±15	175±25
$^{108}\text{Cd}$	120±30	1.16±0.40	4.75±1.25	105±10	125±20
$^{110}\text{Cd}$	155±20	0.28±0.07	4.0 ±0.9	71±6	80±15
$^{111}\text{Cd}$	20±4	(0.5)	3.0 ±1.0	(160)	
$^{112}\text{Cd}$	190±25	0.50±0.10	4.4 ±1.0	77±5	90±20
$^{113}\text{Cd}$	21±4	(0.5)	2.2 ±0.8	160±20	
$^{114}\text{Cd}$	235±35	0.64±0.16	3.5 ±1.0	53±4	70±10
$^{116}\text{Cd}$	390±90	0.16±0.05	2.8 ±0.8	47±4	70±10
$^{134}\text{Ba}$	230±60	0.60±0.15	0.90±0.25	120±20	(180)
$^{135}\text{Ba}$	40±6	0.9 ±0.3	0.8 ±0.2	135±25	
$^{136}\text{Ba}^*$	920±200	1.08±0.3	0.07±0.06	100±20	
$^{137}\text{Ba}$	380±70	0.43±0.10	0.30±0.15	80±15	
$^{138}\text{Ba}^*$	6300±1700	1.0 ±0.4	0.03±0.02	55±20	45±7
$^{139}\text{La}$	208±10	0.76±0.13	0.3 ±0.1	55±6	40±7
$^{140}\text{Ce}^*$	3200±800	1.54±0.53	0.32±0.12	35±9	30±6
$^{141}\text{Pr}^*$	102±20	1.72±0.25	0.7 ±0.3	88±9	
$^{142}\text{Nd}^*$	790±125	1.40±0.35	0.70±0.05	50±8	46±5
$^{143}\text{Nd}$	35±4	3.1 ±0.5	1.0 ±0.4	86±9	
$^{144}\text{Nd}^*$	525±100	3.9 ±1.0	0.8 ±0.3	47±5	
$^{145}\text{Nd}$	19±2	5.2 ±0.9	0.8 ±0.4	87±9	
$^{146}\text{Nd}$	290±80	3.5 ±0.9	1.1 ±0.4	51±6	
$^{148}\text{Nd}$	170±35	2.7 ±0.8	0.60±0.20	46±5	

\*New or modified results

Values in parenthesis are preliminary or estimated values

3.1.3 Neutron capture cross section of  $^{57}\text{Fe}$  (B.J. Allen,  
A. R. de L. Musgrove, R. B. Taylor\*, R. L. Macklin)

The neutron capture cross section of  $^{57}\text{Fe}$  was measured with 0.2% energy resolution from 2.5 to 200 keV. s-wave resonances were fitted in a two channel multi-level analysis of the elastic and inelastic scattering cross sections. A correlation was observed between the s-wave reduced neutron widths and the corresponding radiative widths, which was consistent with the expected valence component.

3.1.4 s-wave resonance parameters in the structural materials

(B. J. Allen, A. R. de L. Musgrove)

The neutron capture cross sections of the isotopes of Ti, Cr and Fe were previously measured at ORELA. s-wave resonances in these data were re-analysed by Monte Carlo methods which accounted for multiple scattering and resonance scattered neutron background effects. A consistent set of radiative and neutron widths has been presented, together with average capture cross sections and s-wave width correlation coefficients.

3.1.5 keV neutron capture in  $^{141}\text{Pr}$  (R. B. Taylor, B. J. Allen,  
A. R. de L. Musgrove, R. L. Macklin)

The neutron capture cross section of  $^{141}\text{Pr}$  was measured with 0.2% energy resolution in the range 2.5 to 200 keV. Resonances were analysed to 13 keV and the average s-wave radiative width was 88 meV with a standard deviation of 27 meV. The s-wave reduced neutron widths and the corresponding radiative widths were not correlated, but the standard deviation of the s-wave radiative widths greatly exceeded that predicted on the statistical model.

3.2 Neutron Capture Research Carried Out in Collaboration with

Brookhaven National Laboratory (M. J. Kenny<sup>†</sup>, C. M. McCullagh<sup>††</sup>,  
M. L. Stelts<sup>††</sup>, H. I. Liou<sup>††</sup>, R. E. Chrien<sup>††</sup>, M. Goldhaber<sup>††</sup>)

Neutron capture spectroscopy was carried out using neutron beams from the 40 MW high flux reactor. Several facilities were used including (1) a fast chopper with a 48 m flight path and (2) a series of filters to provide tailored beams at thermal energy, 2 and 24 keV.

3.2.1 Gamma rays from the 5.9 keV resonance in  $^{27}\text{Al}$

Absolute partial radiative widths were measured for neutron capture in the 5.9 keV p-wave resonance in  $^{27}\text{Al}$ . The resonance capture occurs through a negative parity state and only E1 transitions were observed with reduced widths below average values. This differed from both thermal capture and the 35 keV s-wave resonance, where enhanced M1 transitions occur.

\*James Cook University, Townsville, Queensland

<sup>†</sup>Visiting scientist at Brookhaven National Laboratory, 1977)

<sup>††</sup>Brookhaven National Laboratory, Long Island, New York 11973, U.S.A.



### 3.2.2 Determination of the spin of the 398 eV resonance in $^{35}\text{Cl}$

The spin-parity of the 398 eV resonance in the capture of neutrons by  $^{35}\text{Cl}$  was determined by the method of particle-gamma directional correlations. Spectra were measured at  $90^\circ$  and  $135^\circ$ . The resonance was shown to have a spin parity of  $2^-$  and the process proceeded predominantly with the channel spin 2.

### 3.2.3 Capture of 2 and 24 keV neutrons by Mn

Neutron capture by Mn was characterised by transitions to a large number of final states with spins in the range 1 to 4 over an excitation range of several MeV. The spectra were indicative of a statistical capture process. There was some degree of similarity between thermal and kilovolt capture.

### 3.2.4 Capture of 2 and 24 keV neutrons by the Zr isotopes

Spectra at 2 and 24 keV were obtained for capture by  $^{91,92,94,96}\text{Zr}$  and  $^{\text{Nat}}\text{Zr}$  (50%  $^{90}\text{Zr}$ ). The Zr isotopes had low capture cross sections and no significant spectra were obtained for capture by  $^{90,96}\text{Zr}$ . The other isotopes showed a relatively small number of transitions to low-lying positive parity states. This was quite different to thermal (s-wave) capture. It was concluded that p-wave capture prevails at kilovolt energies and that decay was by electric dipole transitions. The binding energy for  $^{94}\text{Zr}(n,\gamma)$  was measured as  $(6462.3 \pm 1.0)$  keV.

### 3.2.5 Capture of 2 and 24 keV neutrons by $^{145}\text{Nd}$

The most significant feature of spectra from capture by  $^{145}\text{Nd}$  was the strong transitions to the second excited state of  $^{146}\text{Nd}$  at 1043.1 keV excitation. While the other transitions were generally consistent with statistical decay process, this transition provided evidence for a single particle capture process.

### 3.2.6 Capture cross section of Th

Interest in thorium as an alternative reactor fuel has created a need for more precise measurement of capture cross sections. This cross section was accurately measured using tailored neutron beams at thermal, 2 and 24 keV energies. Cross sections were obtained relative to a gold standard by careful measurement of gamma activity from decay after neutron irradiation. Respective values at thermal, 2 and 24 keV are:  $(7.37 \pm 0.08)$ ,  $(1.91 \pm 0.10)$ ,  $(0.538 \pm 0.014)$  b.

### 3.2.7 Symmetry of $^{10}\text{B}(n,\alpha)^7\text{Li}$ yield

The reaction  $^{10}\text{B}(n,\alpha)^7\text{Li}$  is frequently used as a neutron flux monitor. If the alpha particle yield is asymmetric, then the flux measurement is dependent on detector angle. Measurements were made at  $45^\circ$ ,  $90^\circ$ ,  $135^\circ$  with a carefully aligned system. For the energies of the tailored beams, the asymmetry was found to be less than 2%.

### 3.3 Resonance Neutron Capture Spectroscopy in $^{28}\text{Si}^+$

(G. Grenier\*, S. Joly\*, J. Voignier\*, J. W. Boldeman)

The valence model<sup>1</sup> has had outstanding success in explaining the initial final state correlations observed in photonuclear cross section and neutron capture. However, the qualitative success has been tempered to some extent by many quantitative failures. Generally, predictions from the valence model underestimate measured transitions. A notable exception was the  $^{28}\text{Si}(n,\gamma)$  and  $^{29}\text{Si}(\alpha,n)$  reactions<sup>2,3</sup> where the measured values for  $p_{3/2}$  resonances exceeded predictions by about a factor of 3. Halderson et al.<sup>4</sup> have suggested that the valence model should be extended to allow valence transitions to occur in the presence of an excited core. Using a shell model formulation of the valence model and introducing the full structure of the initial and final states, they have calculated the various transition strengths for the two reactions and thereby found better correspondence with existing experimental data.

To provide a more sensitive test of this hypothesis, the resonance  $\gamma$ -ray spectra for the two strongest  $p_{3/2}$  resonances in the  $^{28}\text{Si}(n,\gamma)$  reaction at 565 and 813 keV were measured with NaI and Ge(Li) detectors at Centre d'Etudes de Bruyères-le-Châtel. The measured absolute spectra were found to be in excellent agreement with the valence model and consequently in disagreement with the two previous experiments. A re-examination of the experimental data from the neutron capture cross section experiment<sup>2</sup> showed that the neutron sensitivity of the  $\gamma$ -ray detector<sup>5</sup> was not adequately taken into account and a revision of the analysis has now produced radiative widths in agreement with the present experiment (Table 3.3). Thus both neutron capture experiments are now in reasonable agreement with the valence model and therefore no longer support the need to extend the valence model to allow transitions in the presence of an excited core.

**TABLE 3.3**  
**COMPARISON OF GROUNDSTATE AND TOTAL RADIATIVE WIDTHS**

Resonance energy (keV)	$\Gamma_{\gamma 0}$ Ref. 3 (eV)	$\Gamma_{\gamma 0}$ Present work (eV)	$\Gamma_{\gamma}$ Ref. 2 (eV)	$\Gamma_{\gamma} = \sum_i \Gamma_{\gamma i}$ Present work (eV)
565	1.8	0.6±0.1	2.9 (1.1±0.4)	1.1±0.2
813	5.3	2.8±0.4	9.7 (6.6±1.1)	5.3±0.8

<sup>+</sup>Work performed in collaboration with Centre d'Etudes de Bruyères-le-Châtel

\*Centre d'Etudes de Bruyères-le-Châtel

<sup>1</sup>Lane, A. M. and Lynn, J. E. (1960) - Nucl. Phys. 17, 563

<sup>2</sup>Boldeman, J. W., Allen, B. J., Musgrove, A. R. de L. and Macklin, R. L. (1976) Nucl. Phys. 269, 397

<sup>3</sup>Jackson, H. E. and Toohey, R. E. (1972) - Phys. Rev. Lett. 29, 379

<sup>4</sup>Halderson, D., Castel, B. and Divadeenum, M. (1976) - Proc. Int. Conf. Interactions of Neutrons with Nuclei, Lowell, Vol. 2, 1433

<sup>5</sup>Allen, B. J., Musgrove, A. R. de L., Macklin, R. L. and Winters, R. R. (1977) - Proc. Specialist Meeting on Structural Materials of Fast Reactors, Geel, Dec. 1977

### 3.4 Neutron Capture Studies at Lucas Heights

#### 3.4.1 Neutron capture cross section of $^{170}\text{Yb}$ (B. J. Allen, D. D. Cohen\*)

The neutron capture cross section of  $^{170}\text{Yb}$  is of particular interest in astrophysics since this nuclide is formed solely by the s-process. An enriched sample of 52.68 g of  $^{170}\text{Yb}_2\text{O}_3$  was obtained on loan from the United States Department of Energy and Moxon-Rae  $\gamma$ -ray detectors were used with the 3 MeV pulsed Van de Graaff accelerator to measure the cross section in the energy range 10 to 70 keV with respect to that of gold.  $\text{Yb}_2\text{O}_3$ , carbon, air and gold samples were irradiated in turn in a 12 min cycle, using a computer-controlled sample changer. A  $^6\text{Li}$  glass monitored the transmitted neutron flux. Time of flight results for  $\text{Yb}_2\text{O}_3$  and the associated background are shown in Figure 3.1, together with the background subtracted capture  $\gamma$ -ray yield.

The 30 keV average capture cross section was found to be  $790 \pm 60$  mb. This result confirms the semi-empirical method<sup>1</sup> used to estimate the  $^{170}\text{Yb}$  cross section from the known cross sections of the heavier isotopes. The ratio of the odd-A cross sections to the interpolated values of the even-A cross sections at  $A = 171$  and  $173$  was found to be constant to 10% (i.e.  $2.9 \pm 0.3$ ), as shown in Figure 3.2. The known isotopic cross sections were then used in an exponential extrapolation to obtain a value of  $770 \pm 150$  mb for  $^{170}\text{Yb}$ .

#### 3.4.2 Branching ratio of $^{176}\text{Lu}$ at astrophysical energies (B. J. Allen, G. C. Lowenthal<sup>†</sup>, J. R. de Laeter<sup>††</sup>)

An earlier measurement of the branching ratio for  $^{175}\text{Lu}(n,\gamma)^{176\text{m}}\text{Lu}$  (with a 3.7 hour half-life) at 30 keV neutron energy, was greatly affected by a fall-off of neutron flux during the exposure. The irradiation was repeated using the  $^7\text{Li}(p,n)$  source at 12 keV above threshold, with care being taken to ensure a uniformity in neutron flux throughout the exposure.

The 88 keV  $\gamma$ -ray was detected by a calibrated Ge(Li) detector whose photopeak efficiency was determined to be  $(87.5 \pm 2.5) \times 10^{-4}$  after a series of source measurements with  $\gamma$ -ray energies ranging from 60 to 400 keV. The neutron flux was obtained from the activity of a thin gold foil, which was measured in a  $4\pi$   $\beta$ - $\gamma$  coincidence counter. The activity of the  $^{176\text{m}}\text{Lu}$  at the end point of the nine hour irradiation was  $(7.55 \pm 0.38) \times 10^4$  Bq per g of  $\text{Lu}_2\text{O}_3$ , resulting in a branching ratio to the long-lived ground state of  $B = 0.46 \pm 0.06$ . Since the half-life of this state is  $3.6 \times 10^{10}$  years, it can be used as an s-process chronometer. The branching ratio so determined is an essential link in the measurement of the age of the universe.

\*Australian Institute of Nuclear Science and Engineering, Lucas Heights

<sup>†</sup>Instrumentation and Control Division

<sup>††</sup>Western Australian Institute of Technology

<sup>1</sup>Allen, B. J., Gibbison, J. H. and Macklin, R. L. (1971) - Advances in Nuclear Physics, Vol. 4, Chapter 4.

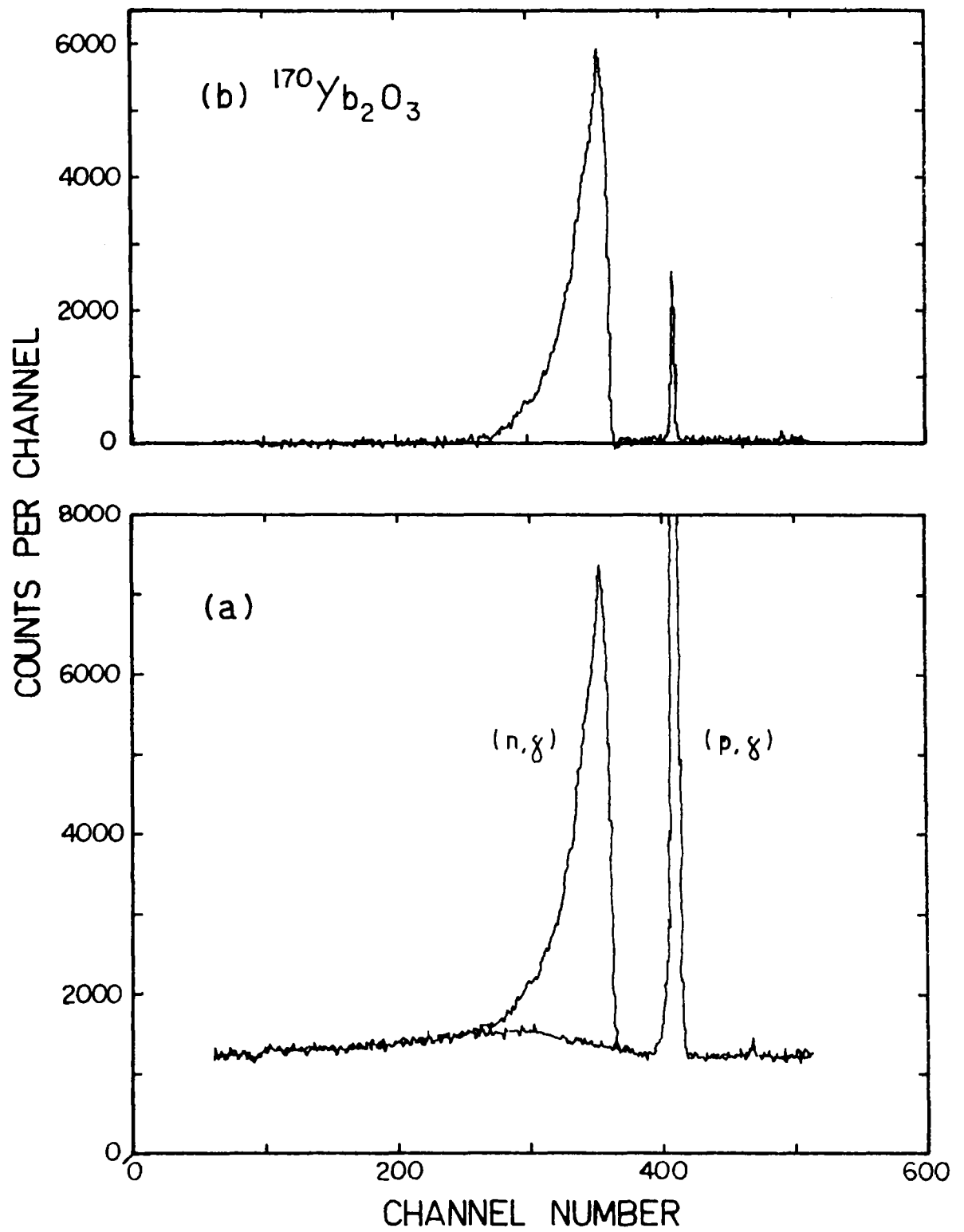


Figure 3.1 Neutron time of flight spectra for  $\text{Yb}_2\text{O}_3$

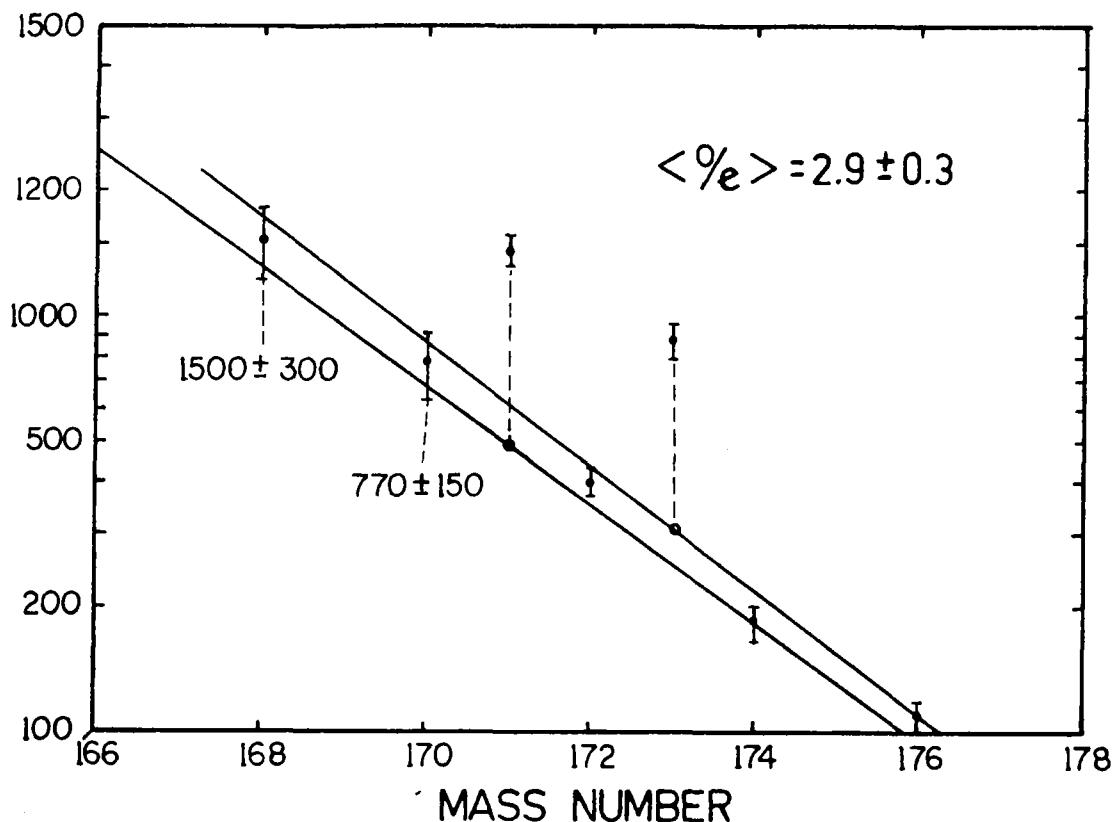


Figure 3.2 30 keV averaged capture cross section as a function of mass number

#### 3.4.3 Radiative widths of scattering resonances

(B. J. Allen, D. D. Cohen, F. Z. Company\*)

Measurements of the radiative widths of scattering resonances for the 27 keV, 49 keV resonances in  $^{19}\text{F}$ , 35 keV resonance in  $^{27}\text{Al}$ , 55 and 57 keV resonances in  $^{28}\text{Si}$  and the 27 keV resonance in  $^{56}\text{Fe}$  are underway. Moxon-Rae detectors were used to measure  $\gamma$ -ray yields from these capture targets, relative to that for gold. These resonances were all found to have substantial prompt background components in high resolution measurements at ORELA and considerable uncertainty is attached to their radiative widths. This problem can be easily overcome by time of flight discrimination of scattered neutrons in these measurements on the pulsed 3 MeV Van de Graaff accelerator.

#### 3.4.4 Neutron capture mechanisms in the 3s size resonance

(B. J. Allen, A. R. de L. Musgrove)

A framework for the partition of s-wave radiative widths into statistical, valence and doorway components was presented for the 3s region.

The statistical calculations used the Gilbert and Cameron level density prescription. The discrete low lying levels were fitted to a constant temperature formula which joins smoothly to the Fermi gas formula at higher energies.

The valence widths were obtained from optical model calculations of contributing  $\gamma$ -ray transitions. These values are dependence on the s-wave reduced neutron

---

\*Ph.D. student, University of Wollongong

widths and the spectroscopic factors of low lying final states.

The s- and p-wave radiative widths are partitioned as follows into statistical (S), valence (V) and doorway (D) components:

$$\begin{aligned}\langle \Gamma_{\gamma p}^S \rangle &= \langle \Gamma_{\gamma p} \rangle ; \\ \langle \Gamma_{\gamma s}^S \rangle &= R^S \langle \Gamma_{\gamma p}^S \rangle ; \\ \langle \Gamma_{\gamma s}^S \rangle &= \langle \Gamma_{\gamma s}^V \rangle + \langle \Gamma_{\gamma s}^D \rangle + \langle \Gamma_{\gamma s}^S \rangle\end{aligned}$$

with variance  $\sigma^2 = \sigma_S^2 + \sigma_V^2 + \sigma_D^2 + \sigma_{ex}^2$

where  $\sigma_S^2 = \frac{2}{v_{eff}} \langle \Gamma_{\gamma s}^S \rangle^2$  ;  $\sigma_V^2 = 2 \langle \Gamma_Y^V \rangle^2$

and  $\sigma_{ex}^2$  is the average experimental variance. The ratio  $R^S$  is obtained from the statistical calculations. It remains to obtain estimates of the doorway component  $\langle \Gamma_Y^D \rangle$  and its variance  $\sigma_D^2$  which reduce the magnitude of the initial state correlation given by

$$\rho_I(\Gamma_{\lambda n}^0, \Gamma_{\lambda Y}) = \frac{\langle \Gamma_Y^V \rangle}{\langle \Gamma_Y^V \rangle + \langle \Gamma_Y^D \rangle} \cdot \left( \frac{\sigma_V^2}{\sigma_S^2 + \sigma_V^2 + \sigma_D^2 + \sigma_{ex}^2} \right)^{1/2}$$

Results of calculations for a range of nuclides in the 3s region are given in Table 3.4. In the main, these results were sensitive to the assumed values of the  $\gamma$ -ray energy dependence ( $E_Y^3$ ) and the ratio  $\Gamma_Y(E1)/\Gamma_Y(M1) = 7$ . Exceptions are  $^{40}\text{Ca}$ ,  $^{45}\text{Sc}$  and  $^{46}\text{Ti}$  where low lying states of mixed parity occur and the ratio of s- and p-wave radiative widths calculated on the statistical model ( $R^S$ ) is close to unity.

Calcium-40 and  $^{45}\text{Sc}$ , because of the insensitivity to the statistical model assumptions, provided strong evidence for the doorway component. In the case of  $^{45}\text{Sc}$  the observed variance of the s-wave radiative widths for a large number of resonances could only be explained by invoking a doorway component with enhanced transitions to a small number of  $\ell_n = 3$  states. This interpretation was supported by  $\gamma$ -ray spectral measurements which showed anomalous intensities to these states. The magnitude and variance of the doorway components in  $^{40}\text{Ca}$  and  $^{45}\text{Sc}$  reduced the expected initial state correlation, yielding good agreement with the measured correlations.

The valence model accounted for the observed variances in  $^{56}\text{Ti}$ ,  $^{48}\text{Ti}$  and  $^{54}\text{Fe}$ , but the valence variance greatly exceeded the experimental value for  $^{60}\text{Ni}$ . A reduction in the valence estimate for  $^{60}\text{Ni}$  would require an increase in  $\langle \Gamma_Y^D \rangle$ , and a lower calculated correlation. With the exception of  $^{46}\text{Ti}$ , good agreement between the expected and observed correlations was obtained, while a larger value of  $\langle \Gamma_Y^D \rangle$  would improve the agreement with  $^{46}\text{Ti}$ .

In  $^{53}\text{Cr}$  the large experimental variance dominated the observed variance and an uncorrelated component is not required to account for the data.

The assumption that  $\langle \Gamma_{\gamma p}^S \rangle \sim \langle \Gamma_{\gamma p} \rangle$  may also cause discrepancies, as observed in  $^{53}\text{Cr}$  and  $^{56}\text{Fe}$ . For  $^{56}\text{Fe}$ , the value  $\langle \Gamma_{\gamma p} \rangle = 0.3$  eV was superseded by elastic scattering measurements at Oak Ridge National Laboratory, which gave  $\ell_n$  and  $J^\pi$  estimates. The new value  $\langle \Gamma_{\gamma p} \rangle = 0.6$  eV cannot be equal to  $\langle \Gamma_{\gamma p}^S \rangle$  since the calculated

statistical width for s-wave resonances (2.1 eV) exceeded the observed value (1.5 eV). Since p-wave spectra are essentially non-statistical in character, the p-wave statistical assumption is invalid. If the same argument holds for p-wave resonances elsewhere in the 3s region, then the magnitudes and variances of the doorway components given in Table 3.4 will be lower limits.

An interesting spin anomaly is apparent in  $^{57}\text{Fe}$ . Low lying states in  $^{58}\text{Fe}$  have spins  $0^+$ ,  $1^+$ ,  $2^+$ , and only states with  $1^+$  can be reached by E1 transition from  $0^-$  resonances, whereas all states are accessible from  $1^-$  resonances. Consequently, statistical and valence components are larger for  $1^-$  resonances, yet the observed radiative widths are smaller.

Results for the 3s region showed evidence for all three capture mechanisms. However, more accurate data are needed for  $^{53}\text{Cr}$  and results for  $^{60}\text{Ni}$  are not consistent with the valence model.

#### 3.4.5 Non-statistical neutron capture mechanisms in $^{139}\text{La}$ and $^{141}\text{Pr}$ (B. J. Allen, A. R. de L. Musgrove)

A detailed study was made of neutron capture in the  $N = 82$  odd-Z nuclides,  $^{139}\text{La}$  and  $^{141}\text{Pr}$ . These nuclides have similar low lying level structure, basically  $f_{7/2}$  wave neutron states coupled to the odd proton, with a p-wave neutron coupled at higher energies. To date, measurements were made at ORELA with R. L. Macklin, of high resolution resonance capture cross sections above 2.5 keV in  $^{139}\text{La}$  and  $^{141}\text{Pr}$ . Capture  $\gamma$ -ray measurements at Lucas Heights with M. J. Kenny et al. on  $^{139}\text{La}$  were carried out with a NaI detector at 210 keV and a Ge(Li) detector at 10-70 keV.

Since valence estimates of  $\sim 1$  meV were negligible compared to the radiative widths and standard deviations: for  $^{139}\text{La}$   $\langle \Gamma_{\gamma} \rangle = 55$  meV, S.D. = 23 meV;  $^{141}\text{Pr}$   $\langle \Gamma_{\gamma} \rangle = 88$  meV, S.D. = 27 meV, a statistical capture mechanism might therefore be expected for these nuclides, despite their  $N = 82$  magic neutron configuration.

However, measurements of the capture  $\gamma$ -ray spectrum in  $^{139}\text{La}$  at 210 keV showed the presence of anomalous  $\gamma$ -ray strength to the  $\ell_n = 3$  low lying states. This observation was interpreted in terms of a 2p-1h interaction, since the unperturbed p-h energies for E1 transitions were similar to the energies of enhanced transitions. High resolution measurements at 10-70 keV confirmed this effect and set an upper limit to the d-wave valence contribution. These results indicated that some E1 strength escapes coupling into the giant dipole resonance, supporting the possibility of a common doorway state for both neutron and photon channels in the threshold region. If this was the case, strong correlations between the neutron and radiative widths might be expected, even though valence effects are negligible.

High resolution capture cross section measurements on  $^{139}\text{La}$  and  $^{141}\text{Pr}$  showed that this was not the case. The observed correlations for large numbers of s-wave resonances were quite consistent with zero. However, large standard deviations of the s-wave radiative widths were observed. These were 42% for  $^{139}\text{La}$  and 31% for  $^{141}\text{Pr}$ , whereas the experimental errors observed in the determination of s-wave radiative widths were 5 to 10%. Calculations of the standard deviation expected for a statistical capture mechanism are readily obtained in the following way.

**TABLE 3.4**  
**PARTITION OF s-WAVE RADIATIVE WIDTHS IN THE 3s REGION**

Target	$J_{\lambda}^{\pi}$	$\langle \Gamma_{\gamma s} \rangle$	$\langle \sigma_{ex}^2 \rangle$	$\sigma_{ob}^2$	$\langle \Gamma_{\gamma p} \rangle$	$R^S$	$\langle \Gamma_{\gamma s}^S \rangle$	$\sigma_s^2$	$\langle \Gamma_{\gamma}^V \rangle$	$\sigma_V^2$	$\langle \Gamma_{\gamma}^D \rangle$	$\sigma_D^2$	$\rho_{I_c}$	$\rho_I$	S.D.
$^{40}\text{Ca}$	$1/2^+$	1.5	0.12	0.90	0.36	0.92	0.33	0.02	0.52	0.54	0.6	0.16	0.4	0.2	0.4
$^{45}\text{Sc}$	$3^-$	0.84	0.01	0.21	0.50	1.08	0.54	0.006	0.10	0.02	0.2	0.17	0.1	0.04	0.13
$^{46}\text{Ti}$	$1/2^+$	1.2	0.08	0.36	0.60	0.94	0.56	0.03	0.53	0.57	0.1	-	1.0	0.43	0.41
$^{48}\text{Ti}$	$1/2^+$	1.4	0.11	1.2	0.33	1.26	0.42	0.03	0.83	1.4	0.2	-	0.8	0.82	0.35
$^{53}\text{Cr}$	$1^-$	1.4	0.42	0.64	1.0	1.83	1.63	0.26	0.22	0.10	-	-	0.39	0.31	0.32
	$2^-$					1.33									
$^{54}\text{Fe}$	$1/2^+$	3.1	1.3	6.8	0.45	2.6	1.2	0.25	1.8	6.7	-	-	1.0	0.79	0.45
$^{56}\text{Fe}$	$1/2^+$	1.5	0.1	0.64	0.6	3.5	2.1	0.84	0.28	0.16	-	-	0.50	0.52	0.36
					0.3		1.1	0.21			0.2	0.17	0.29		
$^{57}\text{Fe}$	$0^-$	2.2	0.71	1.96	0.52	1.7	0.88	0.17	0.17	0.06	1.1	1.0	0.02	0.57	0.51
	$1^-$	1.7	0.30	1.69	0.62	2.8	1.53	0.22	0.54	0.58	-	0.64	0.58	0.66	0.33
$^{60}\text{Ni}$	$1/2^+$	1.4	0.02	0.04	0.23	1.72	0.40	0.03	0.65	0.85	0.4	-	0.65	0.71	0.26



The summation of E1 and M1 transitions to allowed final states is of the form:

$$\Gamma_{\gamma}(J^{\pi}) \propto D_J \cdot \sum_{\mu} [E_{\gamma\mu}^n(E1) + R E_{\gamma\mu}^n(M1)]$$

where  $R = 0.14$  is the assumed ratio of M1 to E1 transition strengths and the exponent  $n$  determines the  $\gamma$ -ray strength function. Discrete low lying levels were used with mostly known  $J_{\mu}^{\pi}$  values. At higher energies, the Gilbert-Cameron formula for the level density was used after adjustments to fit the constant temperature formula at low excitations and the observed resonance spacing  $D_J^{\pi}$ . The statistical model assumption is that the average transition strength to final state is independent of the configuration of the final state.

The observed variance of the s-wave radiative widths is given by

$$\begin{aligned} \sigma_{\gamma}^2 &= \bar{\Gamma}_{\gamma}^2 (\sigma_{\gamma \text{ obs}}^2 / (g \bar{\Gamma}_{\gamma})^2 - \sigma_g^2 / \bar{g}^2) \\ &= \sigma_{\text{exp}}^2 + \sigma_S^2 + \sigma_V^2 + \sigma_D^2 \end{aligned}$$

where the subscripts denote the experimental errors, the uncertainty in the  $g$  factor and the variance attributed to the statistical, valence and doorway components of the  $\gamma$ -ray spectrum. The valence component is very small and is excluded. Statistical calculations were made for both  $E_{\gamma}^3$  and  $E_{\gamma}^5$   $\gamma$ -ray energy dependences and the relative standard deviations ( $\sigma_g / \bar{g}$ ,  $\sigma_i / \bar{\Gamma}_{\gamma}$  in per cent) are given below.

La	obs %	exp %	g %	S %		D %	S %		D %
La	42	10	13	$E_{\gamma}^3$	10.3	37	$E_{\gamma}^5$	22	32
Pr	31	10	17		7.7	23		19	15

The  $E_{\gamma}^3$  calculations clearly point to a doorway component as the source of the large variance observed for s-wave radiative widths. Enhanced transitions to the low lying  $\ell_n = 3$  states, as observed in  $^{139}\text{La}$ , can readily account for this variance. The doorway variance is reduced in the  $E_{\gamma}^5$  calculation, particularly for  $^{141}\text{Pr}$ , where the statistical variance is dominant.

The observation of anomalous  $\gamma$ -ray transitions to the low lying  $\ell_n = 3$  states in  $^{141}\text{Pr}$  capture spectra should confirm, as in  $^{139}\text{La}$ , the presence of  $\gamma$ -ray doorway states. Since resonance width correlations are not present and evidence for a neutron doorway state has been found in  $^{139}\text{La}$ , the proposed  $\gamma$ -ray doorway state must be weakly coupled to the entrance channel.

### 3.5 Fission Studies

#### 3.5.1 $^{252}\text{Cf}$ spontaneous fission neutron spectrum

(J. W. Boldeman, D. Culley, R. Cawley)

The fission neutron spectrum from the spontaneous fission of  $^{252}\text{Cf}$  has been recommended as one of the two standard neutron fields. The spectrum is best approximated analytically by a Maxwellian distribution,  $N(E) \propto \sqrt{E} \exp(-E/T)$ , where  $T$  is the temperature. The two characteristics of the spectrum required to high accuracy because of their status as a standard, are the temperature of the Maxwellian

and a measure of the deviation of the actual spectrum from the analytical representation.

Despite a considerable number of different measurements, neither of these characteristics can be said to be entirely settled. A number of years ago, values for the average energy of the spectrum ( $\bar{E} = \frac{3}{2} T$ ) split into groups: one centred near 2.13 MeV and the other near 2.35 MeV. The more recent measurements strongly support the lower figure and a value of  $2.13 \pm 0.02$  MeV was recommended for the average energy. Nevertheless, further confirmation is desirable. For the detailed shape of the spectrum and the magnitude of any deviation from the Maxwellian shape, no overall consensus has been achieved. For the region above 8 MeV, for example, the experimental evidence is inconsistent.

A measurement of the spontaneous fission neutron spectrum of  $^{252}\text{Cf}$  using the time of flight technique has been completed for the energy region 600 keV to 15 MeV. A plastic scintillator with experimentally determined absolute efficiencies was used as the neutron detector. The fission counter was a fast ionisation chamber.

The novel feature of the experiment was the simultaneous recording, event by event, of both the neutron time of flight time and the corresponding neutron detector response. With this additional data, the spectrum for a particular time of flight interval corresponding to a particular neutron energy can, after the subtraction of the time-dependent and independent background, be compared with the previously measured neutron response. This comparison provides confirmation that the background has been adequately taken into account, applies an additional check on the accuracy of the timing calibration and adds confidence in the absence of systematic errors.

The time-dependent background was determined using the interval of the time of flight spectrum preceding in real time the prompt  $\gamma$ -ray peak. The time-dependent background was determined using a polythene shadow bar (90 cm thick) to attenuate totally the direct flight neutrons.

Typical time of flight spectra are shown in Figure 3.3 for a number of different thresholds for one of the five different measurements. In the analysis of such data, the response spectra for intervals of five channels in the time of flight spectrum were summed. A five-channel increment was chosen as this corresponded approximately to the experimental time resolution. From the timing calibration data, the relativistically corrected lower and higher energy points for each five-channel increment of the time of flight scale were obtained. The data were corrected for all types of dead time loss (e.g. on the stop and start lines of the time of flight system), the backgrounds were subtracted and the detector count rates corrected for the appropriate neutron detection efficiencies.

The corrected data from the above procedure consisted of increments of the fission neutron spectrum between the higher and lower energy cut-off points of the five-channel increment of the time of flight spectrum. Consequently, the corrected data were fitted to the integral of a Maxwellian spectrum between the energy limits for each data segment to obtain the temperature. The average value of the temperature describing the Maxwellian was  $1.406 \pm 0.013$  MeV, where the experimental error includes all known forms of possible experimental error. Figure 3.4 shows a typical fit to one of the measurements.

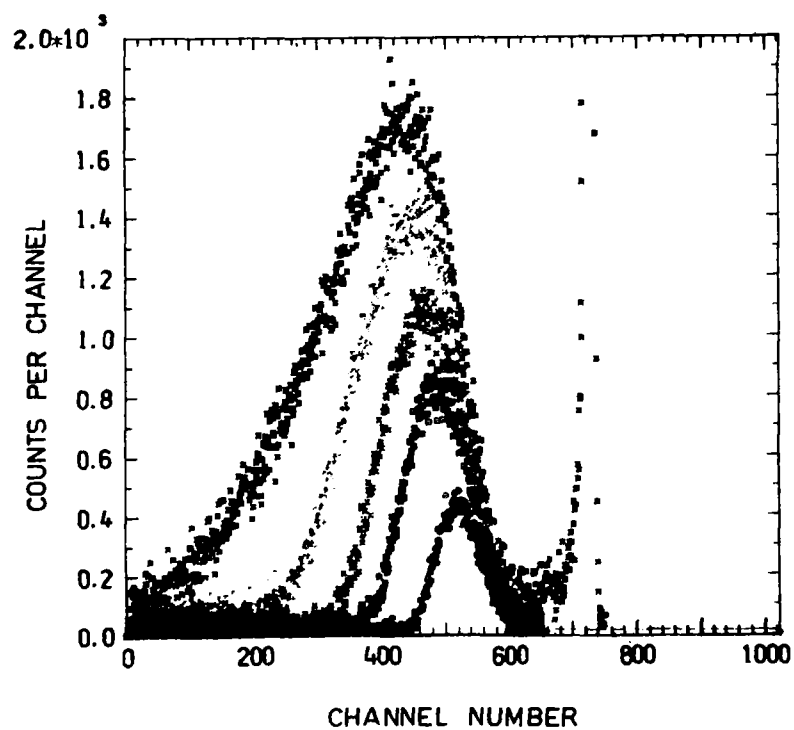


Figure 3.3 Time of flight neutron spectra at different bias settings

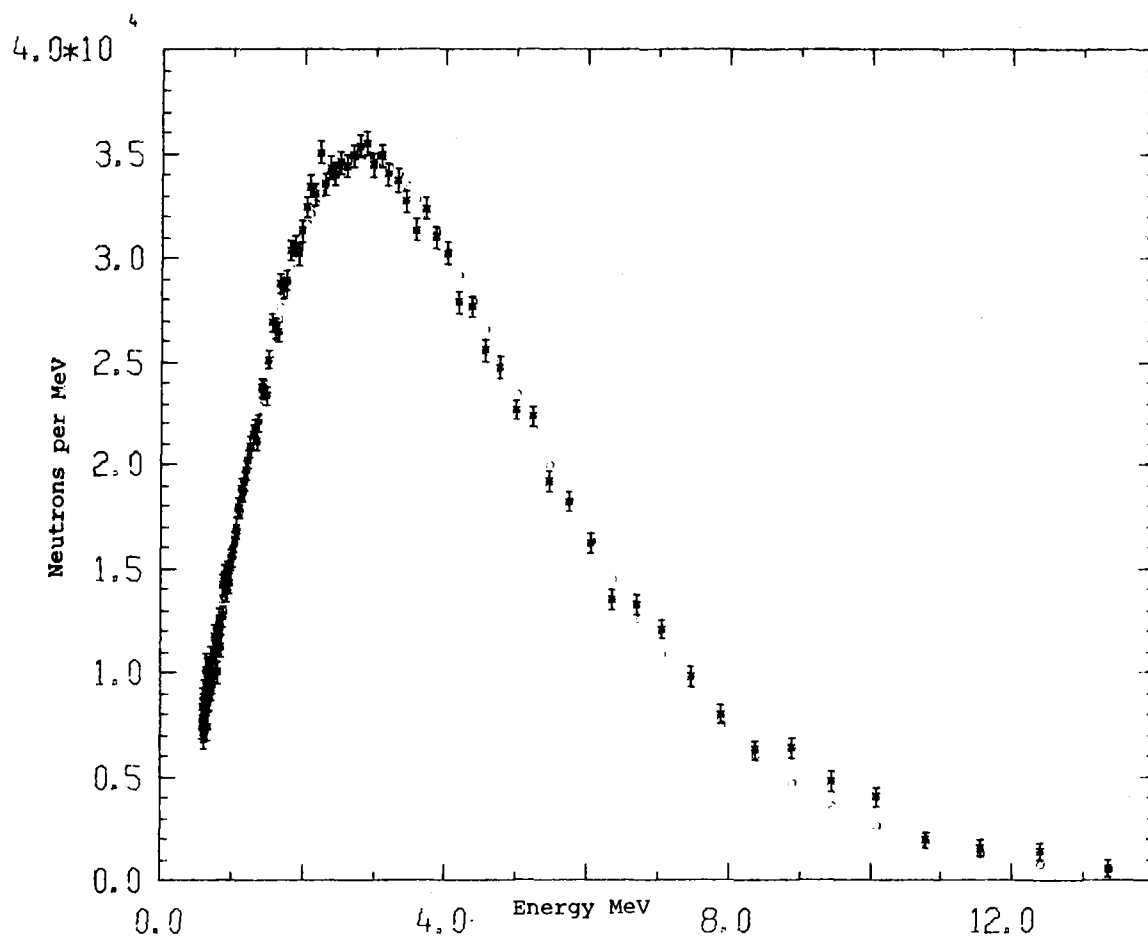


Figure 3.4  $^{252}\text{Cf}$  spontaneous fission neutron spectrum

One of the prime objectives of the present experiment was to determine the extent of any deviation from the Maxwellian shape. For that part of the fission neutron spectrum between 1 and 6 MeV, the experimental data from each of the five measurements are consistent with the Maxwellian shape to better than  $\pm 2\%$ , which is the experimental limit imposed by the accuracy of the absolute calibrations. Above 8.5 MeV (Figure 3.5) the combined experimental data show a significant but very small positive deviation from the Maxwellian shape ( $T = 1.4065$  MeV).

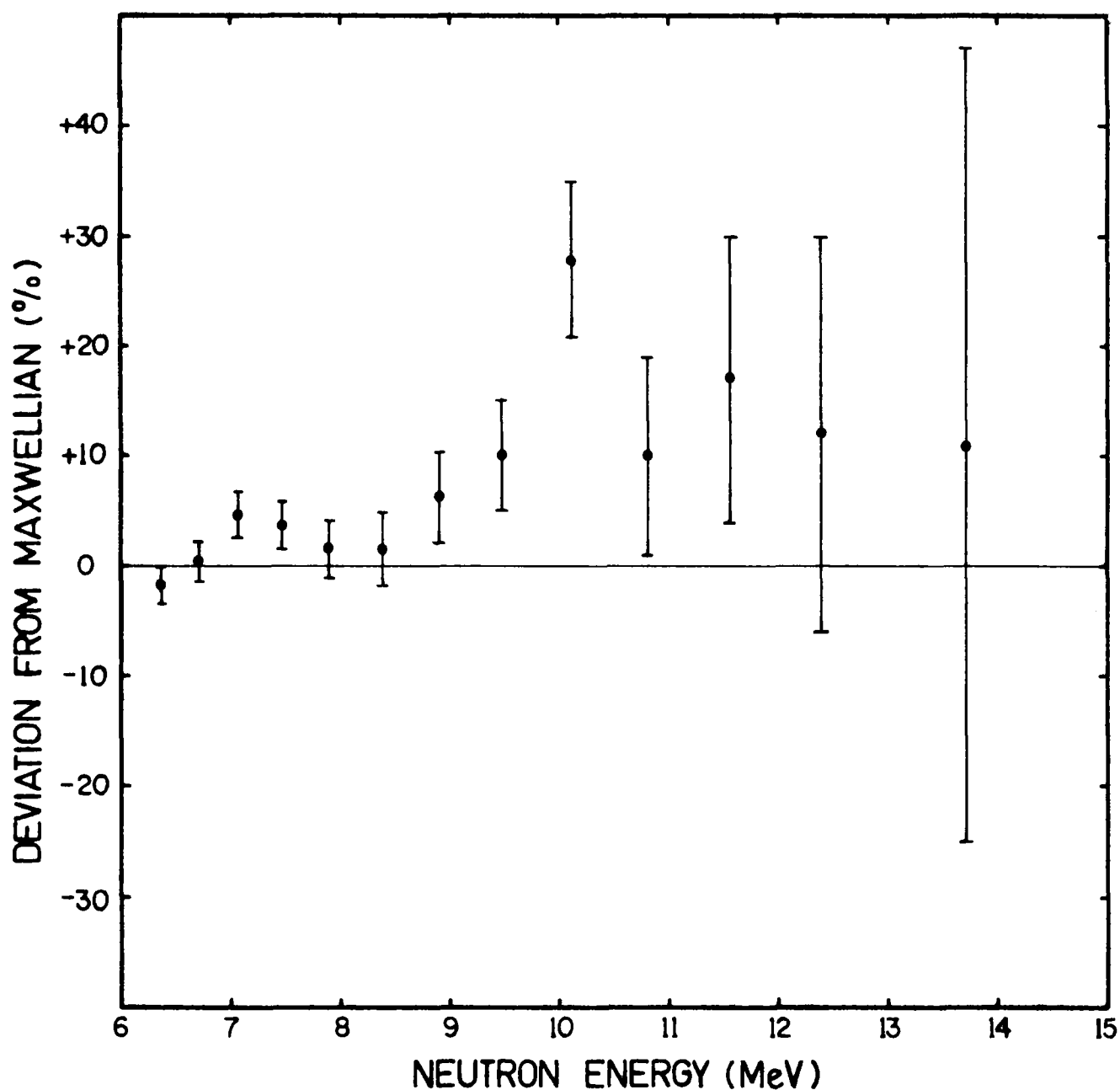


Figure 3.5 Deviation of  $^{252}\text{Cf}$  spontaneous fission spectrum from Maxwellian distributions (6 to 14 MeV)

### 3.5.2 Neutron detector efficiency (D. Culley, J. W. Boldeman)

Measurements of fission neutron spectra require that the detector efficiency be known. The neutron detection efficiency of a number of plastic scintillators have been determined absolutely in the energy range 0.5 to 16 MeV. For the neutron energy range 2 to 10 MeV, the associated particle method was employed, using the experimental system of Bartle and Quin<sup>1</sup>, installed on the 12 MeV tandem Van de Graaff accelerator at the Australian National University. The estimated accuracy of the absolute calibration in this energy region was  $\pm 2\%$ . Between 0.5 and 2.0 MeV, the efficiency was determined relative to a long counter, using the  $^7\text{Li}(p,n)$  and  $\text{T}(p,n)$  variations and normalised to the absolute associated particle value at 2.0 MeV.

In all of the efficiency measurements, the response of the neutron detector was determined for each incident neutron energy. Thus efficiency curves have been obtained at all incident energies for a wide range of lower level biases. Figure 3.6 shows absolute efficiencies of the neutron detector for a number of different bias settings.

For the energy region 10 to 16 MeV the neutron detection efficiencies are presently based on calculation, but it is intended to extend the associated particle measurements into this region.

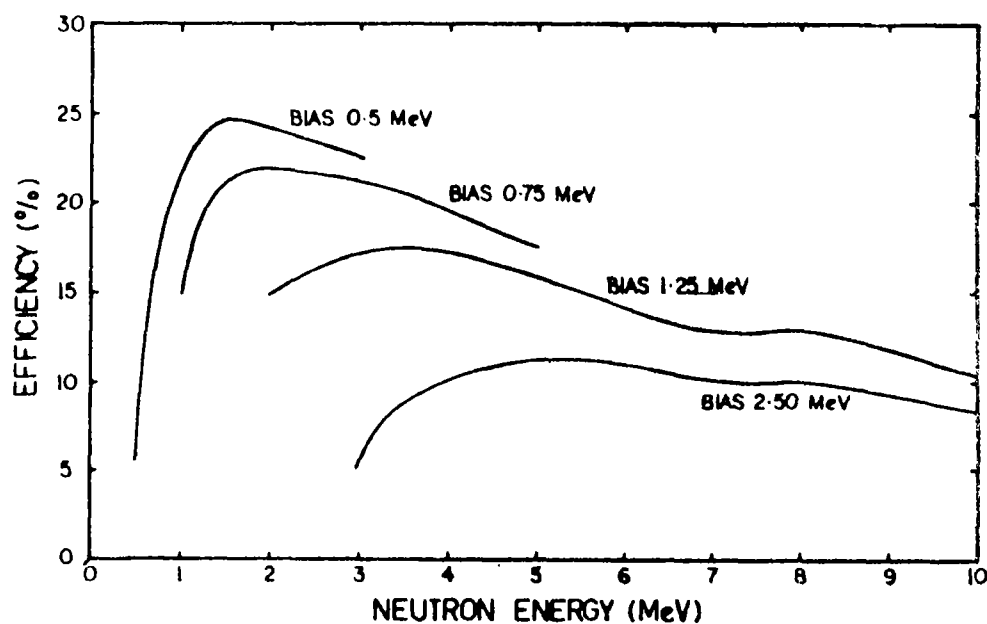


Figure 3.6 Absolute efficiency of neutron detector from 2 to 10 MeV

<sup>1</sup>Bartle, C. M. and Quin, P. A. (1974) - Nucl. Instr. 121, 119

### 3.5.3 Fission barrier for the thorium isotopes

(J. W. Boldeman, R. L. Walsh)

An interesting problem in fission at the present time is the question of the shape of the fission barriers for the thorium isotopes. Much of the apparently anomalous fission data for the thorium isotopes can be explained (Blons, et al.<sup>1</sup>; Gavron et al.<sup>2</sup>) if, as has been predicted by Möller and Nix<sup>3</sup>, the outer barrier of the double-humped fission barrier splits into two separate peaks separated by a fairly shallow valley. Our previous studies (Caruana, et al.<sup>4</sup>) of the fission fragment angular distributions for neutron fission of  $^{232}\text{Th}$  supported this hypothesis. It was found impossible to obtain a simultaneous fit to the fission fragment angular distributions and the fission cross section with a double-humped fission barrier. However, with a triple-humped barrier it was possible to obtain a simultaneous fit to both sets of data, although a large number of fission bands were required ( $D_{K\pi} \approx 60$  keV) if all bands were restricted to the same triple-humped shape. Alternatively, both sets of data could be fitted simultaneously with far fewer bands if a combination of double and triple-humped barriers were allowed.

Studies of neutron fission of  $^{230}\text{Th}$  provided a further opportunity to study this matter. A very recent measurement of the neutron fission cross section of  $^{230}\text{Th}$  by Blons et al.<sup>5</sup> has also been interpreted as evidence of a triple-humped barrier shape for the compound nucleus of  $^{231}\text{Th}$ .

Our fission fragment angular distribution studies have been extended to  $^{230}\text{Th}$ . Measurements of the angular distribution around the large resonance at 715 keV in the cross section have been made with 5 keV energy resolution. Measurements have also been made to 1 MeV with slightly poorer energy resolution.

Presently, the analysis of our angular distribution data support the work of Blons et al., although there are important differences in the details of the analysis. However, the most significant aspect of the study has come from the attempt to provide a complete fit to all experimental data from 0.6 to 1.4 MeV. It has been found impossible to fit the data assuming a constant barrier shape for the different fission bands. However, a fit appears possible to all data with a small number of fission bands of slightly different shape.

### 3.5.4 Measurement of kinetic energies of $^{239}\text{Pu}$ , $^{235}\text{U}$ fission fragments in the resonance region

(R. L. Walsh, J. W. Boldeman, M. M. Elcombe\*)

#### (a) $^{239}\text{Pu}(n,f)$

For compound nuclei which have their outer fission barrier the same height as or higher than their inner barrier, the collective energy at the saddle point is

---

<sup>1</sup>Blons, J., Mazur, C. and Paya, D. (1975) - Phys. Rev. Lett. 35, 1749.

<sup>2</sup>Gavron, A., Britt, H. C. and Wilhelmy, J. B. (1976) - Phys. Rev. 13, 2577.

<sup>3</sup>Möller, P. and Nix, J. R. (1973) - Proc. 3rd IAEA Symp. Physics and Chemistry of Fission, Rochester, N.Y., 1; 103.

<sup>4</sup>Caruana, J., Boldeman, J. W. and Walsh, R. L. (1977) - Nucl. Phys. 285, 205.

<sup>5</sup>Blons, J., Mazur, C., Paya, D. and Rèbray, M. (1978) - Phys. Rev. Lett. (to be pub.)

\*Materials Division

only weakly coupled to the nuclear degrees of freedom at scission. Changes in the collective energy appear directly as changes in fragment kinetic energy (Boldeman et al. 1976<sup>1</sup>).

However, for nuclei with the outer barrier lower than the inner, the situation is not clear. Measurements of neutron multiplicity ( $\bar{\nu}$ ) for  $^{239}\text{Pu}(n,f)$  in the resonance region have found that  $\bar{\nu}$  for a  $J = 0^+$  resonance is 0.5 to 2% larger than  $\bar{\nu}$  for a  $J = 1^+$  resonance<sup>2,3</sup>. A change in  $\bar{\nu}$  of this size suggests strong coupling between collective and nucleonic degrees of freedom. In terms of energy, this change is equivalent to 0.13 to 0.6 MeV and should be seen as a change in the average total kinetic energy ( $\bar{E}_K$ ) of the fission fragments. However, a fragment kinetic energy measurement (Toraskar and Melkonian 1971<sup>4</sup>) using filtered beams in the resonance region, found a kinetic energy change of  $1.5 \pm 0.1$  MeV. This result implies that the coupling is weak.

To clarify the situation, we are measuring the variation of  $\bar{E}_K(E_n)$  for  $^{239}\text{Pu}(n,f)$  for  $E_n = 0.005$ – $0.4$  eV, the energy region studied in ref. 3. A double-energy configuration with surface barrier detectors is used. The target is  $12 \mu\text{g cm}^{-2}$   $^{239}\text{Pu}$ , electrosprayed over an area of  $1.3 \text{ cm}^2$ . Data is recorded, event by event, on magnetic tape.

A triple axis spectrometer is used to provide a monoenergetic neutron beam from the HIFAR reactor. The beam flux incident on the target was measured at  $3.8 \times 10^4$  neutrons  $\text{cm}^{-2} \text{ s}^{-1}$  with a 3.4% FWHM beam energy resolution at  $E_n = 0.296$  eV. Beam contamination from lower order Bragg scattered wavelengths (i.e. higher energy neutrons) is  $<5\%$ .

We have measured  $\bar{E}_K$  and mass yield distributions for  $E_n = 0.296$  eV and  $0.033$  eV. At  $0.296$  eV 90% of the fission occurred through the  $(J,K,\pi) = (1,1,+)$  collective level, whereas at  $0.033$  eV, 45% occurred through  $(1,1,+)$  and 55% through  $(0,0,+)$  the ground state band. The fact that only two individual K bands are operating and that each band contributes one and only one J level to the fission strength, makes the  $^{239}\text{Pu}(n,f)$  system in this energy range a most powerful tool for probing fission collective properties. For almost all other  $(n,f)$  systems (with no beam polarisation or target alignment) the K and J contributions are not seen separately.

Figure 3.7 shows the pulse height distribution from a single surface barrier detector for  $E_n = 0.296$  eV. Figure 3.8 shows the total (i.e. summed) pulse height distribution from two complementary fragments. The mean of this peak defines the value of  $\bar{E}_K$ . Our preliminary data indicate a difference of  $\sim 0.4$  MeV in  $\bar{E}_K$  between fission via (pure)  $J = 0^+$  or  $1^+$  states, a result similar to that of Leonard (1976)<sup>3</sup>.

<sup>1</sup>Boldeman, J. W., Bertram, W. K. and Walsh, R. L. (1976) - Nucl. Phys. A265, 337.

<sup>2</sup>Fréhaut, J. and Shackleton, D. (1973) - Proc. 3rd IAEA Symp. Physics and Chemistry of Fission, Rochester, N.Y., 1, 103.

<sup>3</sup>Leonard, B.R., Jr. (1976) - private communication.

<sup>4</sup>Toraskar, J. and Melkonian, E. (1971) - Phys. Rev. C4, 267.

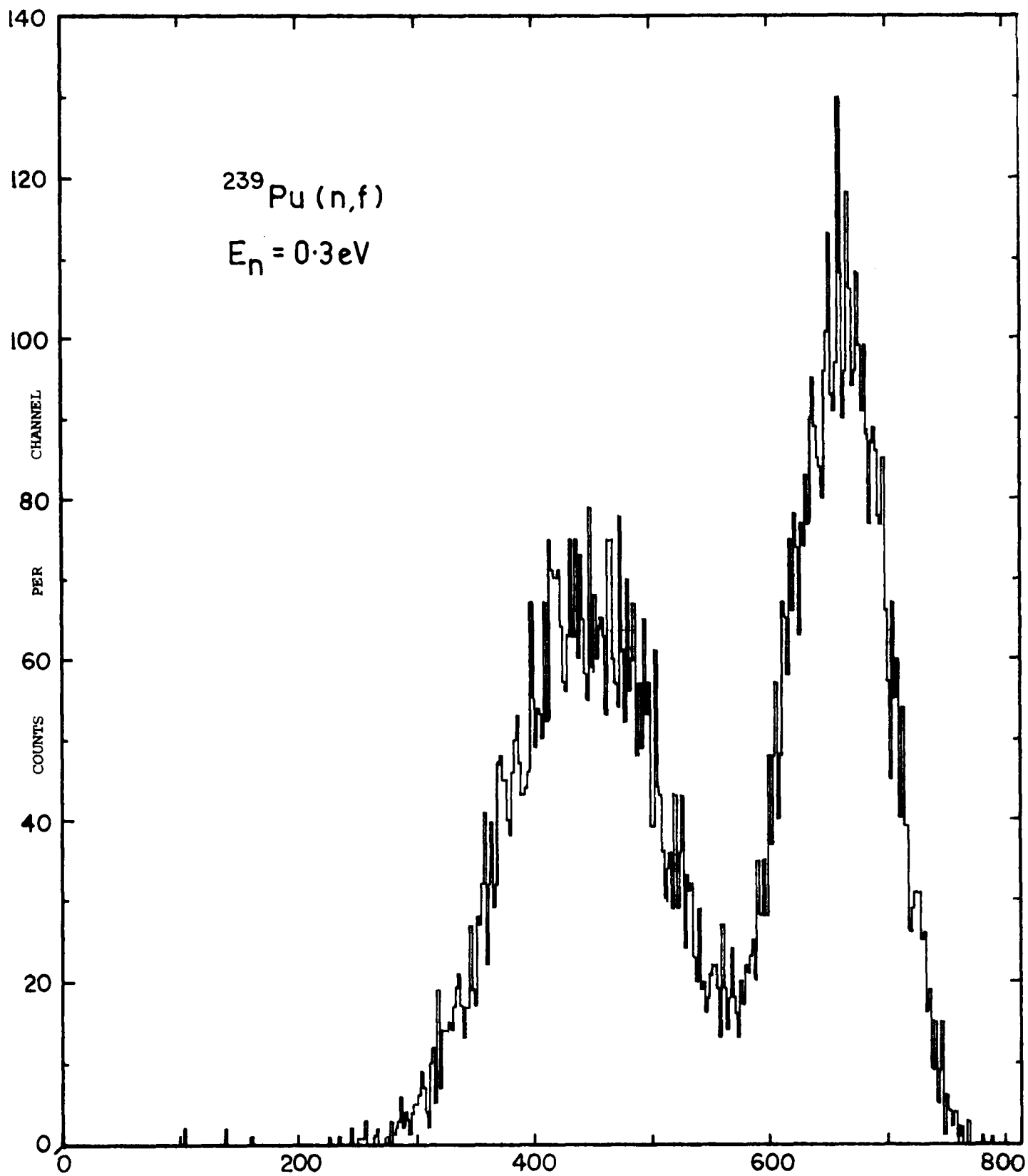


Figure 3.7  $^{239}\text{Pu}(n,f)$ : single detector fission fragment pulse height distribution



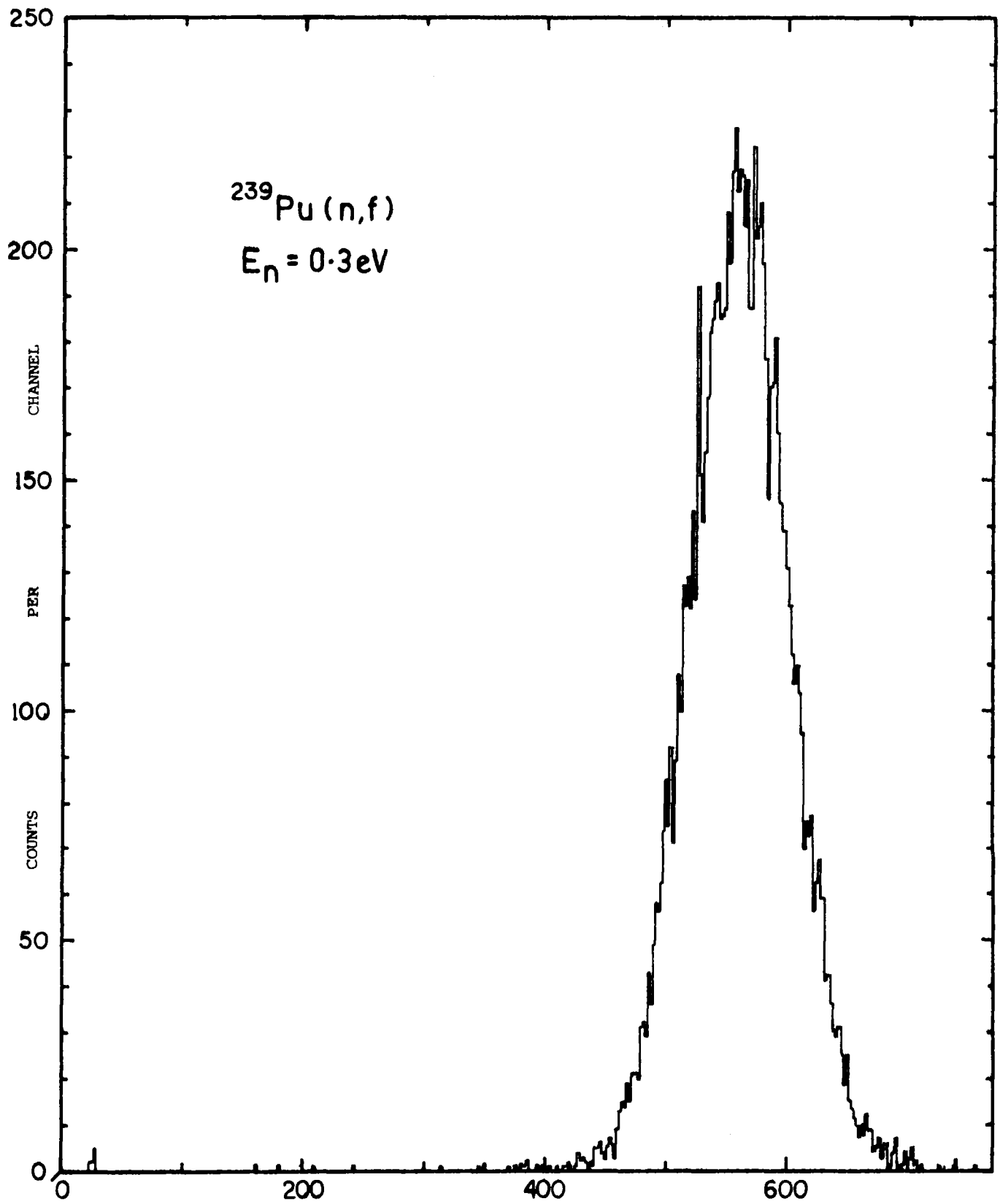


Figure 3.8  $^{239}\text{Pu}(n,f)$ : total pulse height distribution  
(summed from two complementary detectors)

(b)  $^{235}\text{U}(n,f)$ 

As a check on the experimental system before the  $^{239}\text{Pu}$  measurement was commenced,  $\bar{E}_K$  for  $^{235}\text{U}(n,f)$  was measured at  $E_n = 0.033$  and  $0.12$  eV. Because of the properties of the saddle point collective levels in the  $^{236}\text{U}$  compound nucleus, no difference in  $\bar{E}_K$  should be expected at these two energies. The measured  $\bar{E}_K$  difference was  $0.025 \pm 0.100$  MeV, thus confirming the accuracy of the experimental system.

3.5.5 Preparation of  $^{239}\text{Pu}$  targets by electro spraying

(R. L. Walsh, I. F. Senior, J. J. Fardy\*)

Plutonium-239 targets for the above fission fragment kinetic energy measurement were prepared by the method of electro spraying. The solution used was  $0.5$  mg/ml plutonium acetate in methanol. Great care was taken to ensure that the solution was totally free of plutonium nitrate, which is hygroscopic. Plutonium acetate targets previously purchased from the Central Bureau for Nuclear Measurements, Geel, Belgium, proved unsuitable for the  $\bar{E}_K$  measurement because of the presence of plutonium nitrate.

A target table was constructed which provided movement in the X and Y directions perpendicular to the spray jet (Z direction). This was to ensure uniform target deposition. Table speeds were:

X direction:  $10 \text{ cm s}^{-1}$  ( $1 \text{ cycle s}^{-1}$ ), i.e. fast movement

Y direction:  $1 \text{ cm min}^{-1}$  ( $1 \text{ cycle per } 10 \text{ min}$ ), i.e. slow movement

The solution was sprayed through a 21G stainless steel hypodermic needle, with its bore constricted by a  $0.018''$  Pt wire. Spray voltages applied to the needle were  $8$  to  $10$  kV. Target backings were  $15 \mu\text{g cm}^{-2}$  VYNS covered by  $10$  to  $15 \mu\text{g cm}^{-2}$  Au-Pd. The apparatus (Figure 3.9) was enclosed in a glove box; the box itself was situated inside a fume cupboard.

Preliminary tests using inactive solutions (e.g.  $\text{CuCl}_2 \cdot 2\text{H}_2\text{O}$  in methanol) showed the average grain size of the deposit to be  $\approx 1 \mu$ . Fission fragment pulse height spectra from a number of plutonium targets ( $12$  to  $18 \mu\text{g cm}^{-2}$ ) (Figure 3.7) showed good peak-to-valley ratios ( $\sim 6:1$ ) and absence of a low energy tail from fragment self-absorption.

The advice of Dr. Pauwels (CBNM) is gratefully acknowledged.

---

\*Chemical Technology Division

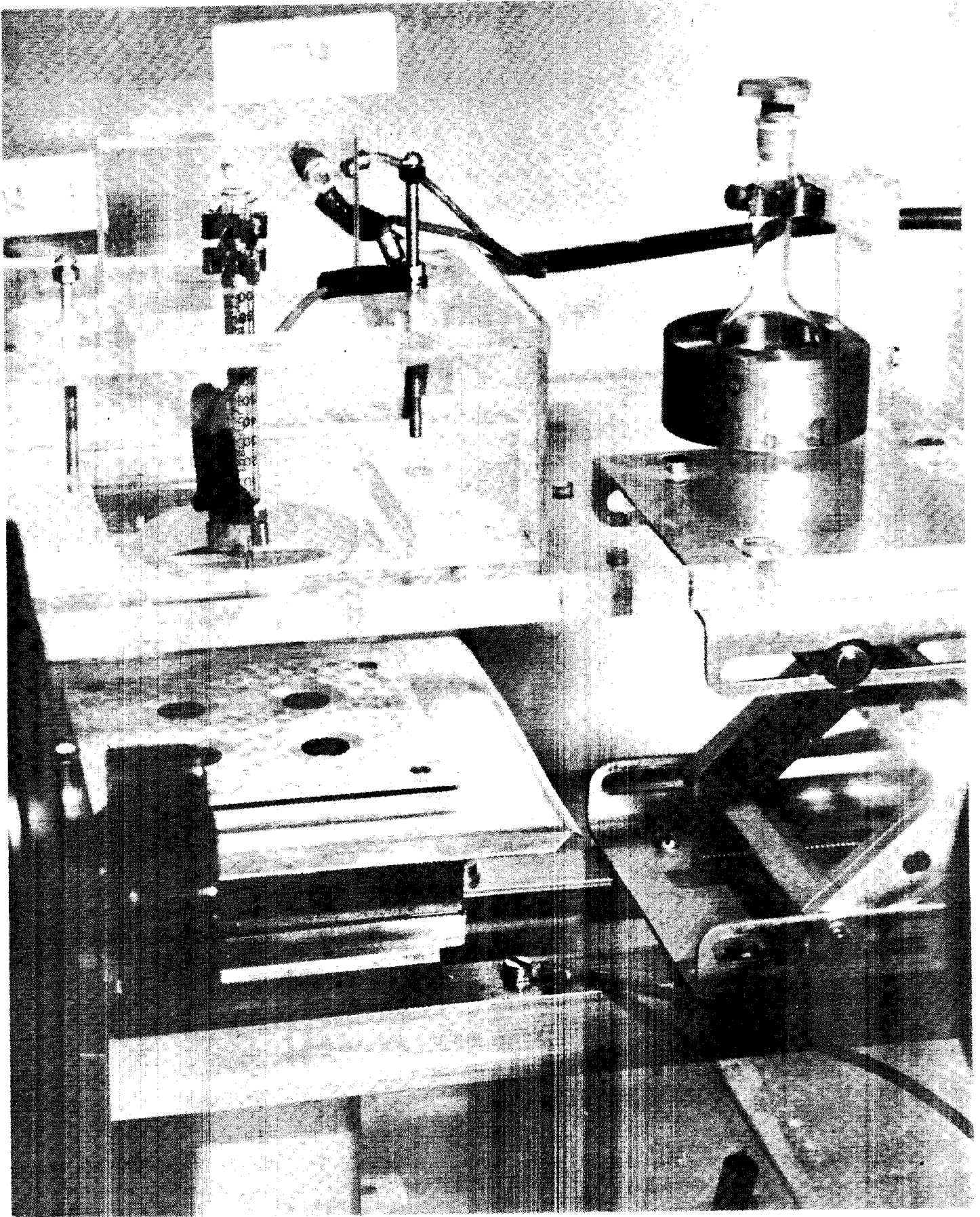


Figure 3.9 Apparatus for electro-spraying of  $^{239}\text{Pu}$

#### 4. NUCLEAR TECHNIQUES

##### 4.1 3 MeV Van de Graaff Accelerator (H. Broe, J. Fallon, J. Fredericks, L. Russell)

The accelerator operated for 3182 hours during the year. Time allocation for each experimental program is shown in Table 4.1. Further trouble was experienced with the alternator bearings. One bearing housing and the alternator journals were rebuilt. The charge carrying belt was also changed after 1500 hours operation as it was thought to be contributing to an out of balance situation in the alternator. The external gas supply problem remains unresolved, but it is expected that the proposed acquisition of a different type of tubing should give satisfactory operation. The performance of the current accelerating tube after 3800 hours operation has been disappointing. It is still necessary to regularly condition the tube for any energy above 2 MeV. The total downtime was 2739 hours, with some maintenance carried out during accelerator operations.

Developmental work during the year included:

- (i) A light pipe filter system as an alternative to wrapping the light pipes in black PVC tape.
- (ii) Improvement of operational safety by the installation of a cell interlock system.
- (iii) Monitoring of cooling oil temperature on the post acceleration deflection unit.

##### Alternator bearings

Bearings continued to be a problem, becoming noisy before reaching their anticipated lifetime. One bearing journal was found to be 0.03 mm eccentric to the other, which is outside the recommended tolerance.

Both bearing journals were ground, hard chromed and reground together to ensure concentricity. The shaft diameter is 50 mm with a tolerance of +0.000 to 0.005 mm. This permits the substitution of roller bearings later, if desired.

A new bronze bearing housing was manufactured. The holes in the other housing, which had previously been drilled for balancing purposes, were blocked with brass plugs and the housing rebalanced.

After assembly, the alternator was dynamically balanced to 6.1 g mm (specification is 10.9 g mm). On previous occasions the alternator units were balanced separately rather than as a whole and this may account for some of the problems which have been encountered. Since rebalancing, no deterioration has occurred in 2300 hours operation. Initially, bearing noises were monitored by Applied Mechanics Section of the Engineering Research Division, at 200 hour intervals. This is no longer considered necessary.

##### External Gas System

The malfunctioning of the plastic gas line connecting the base or earth potential end of the machine to the high potential terminal has now been overcome by weaving the line through the column to the accelerating tube connection springs. The gas line now lies in a uniform field.

TABLE 4.1

ACCELERATOR TIME ALLOCATION OCTOBER 1, 1977 TO SEPTEMBER 30, 1978

Category	Experiment Title	Personnel	Origin	Running Time (hours)
Applications	Elemental Analysis:			
	PIGMY/PIXE/RBS	Bird, Scott, Russell	Physics	516
	PIXE	Duerden, Clayton, Company	Physics/AINSE	288
	PIXE/RBS	Cohen et al.	AINSE	384
Neutron Transport	Pulsed spectra	Whittlestone	Physics	544
Neutron Data	Fission, fission fragments	Boldeman, Walsh	Physics	443
	$^{252}\text{Cf}$	Culley, Boldeman	Physics	103
	Capture cross sections	Allen, Cohen, Company	Physics/AINSE/Wollongong	734
AINSE Projects	Crystals	Anderson	UNSW	45
	(p, $\gamma$ ) spectroscopy	Lasich	Queensland	36
Tests				91

Total running time 3182  
Maintenance and development 2739  
Unused time 2839

Although the functioning problem has been overcome, another fault has become evident. The nylon tube used (dimensions 0.250" OD and 0.169" ID) exhibited high permeability and tank gas polluted the gas used for ionisation. Thus the beam produced by the ion source contained heavy ions which overloaded the focusing power supplies, with the consequent destruction of einzel lens dropping resistors.

#### Light Pipe Filters

In the bunched countdown and bunched modes, fast pulses, typically 100 ns, are transmitted via Perspex light pipes over a distance of approximately 2 m. The pulses are produced by a LED source with peak spectral emission at 560 nm and sensed by photomultipliers with peak response at 400 nm. The light pipes have been optically insulated with black PVC tape. This prevented such events as tank sparks or corona discharge interfering with the pulsed signal. Problems occurred when the insulation broke down along the length of the light pipe and caused terminal voltage instability (see AAEC/PR43-PD).

The installation of a combination of filters at the photomultiplier end of the light pipe avoided the problem associated with the PVC tape. The combination of filters, spectral emission and spectral response ensured that only 14% of the total light emitted by the LEDs is seen by the photomultiplier; less than 1% of this transmitted light lies outside 560±10 nm. Thus very little of any light source other than the one of interest is seen by the photomultipliers.

Testing of the new system with the pressure tank-off was carried out by placing a sheet of black plastic over the light pipes; even without plastic, the photomultipliers did not saturate under strong fluorescent lighting. This system is still in the testing stages, but all indications are that it will continue working successfully.

#### Cell Interlock System

The system whereby the responsibility for locking the accelerator cell door rests with the operator is being revised. The proposed new system is that the cell door will be electrically interlocked by a key at the control desk whenever the drive motor is running. It will operate as follows:

1. If radiation (gamma or neutron) exceeds a preset level and the interlock is released, the drive motor will trip.
2. If radiation does not exceed the preset level, releasing the interlock key will not trip the drive motor and the cell may be entered.
3. To protect a person accidentally locked in the cell, a loud and distinctive siren will sound for 30 seconds whenever the radiation rises above the preset level. A door release button will be located at the outer door. This door will automatically relock on exit. There exists also an emergency shutdown switch within the cell.
4. If someone has entered the cell under low radiation conditions and the radiation rises to the preset level, the drive motor will trip.

Further operational safeguards include: use of a small source to activate radiation monitors; microswitch supervision of door position so that the locking solenoid can only operate when the door is fully closed.

Panel lights will indicate the condition of the interlock circuitry.

#### Post Acceleration Deflection Cooling Oil Monitoring

The two output valves in the post acceleration deflection unit are oil cooled and loss of coolant will result in destruction of one or both valves. An integrated circuit sensing device was constructed and mounted on a coil heated slug. Oil flow normally keeps the slug cool; inadequate flow in the coil causes the slug temperature to rise rapidly and operate trip level (typically 80°C). The time constant of this device is approximately 10 seconds from loss of coolant.

#### Minibeam

(M. D. Scott, A. van Heugten)

The sub-millimetre diameter beam obtained by the use of a collimating aperture within the target chamber was used for the study of specific features in samples, including a search for regions of concentrated impurities in germanium ingots. In these measurements, problems have been encountered in the measurement of beam currents at nanoamp levels.

The possibility of isolating the target from the chamber is complicated by secondary and flood electron leakage between target, filament, chamber and collimating aperture. Attempts to magnetically confine these electron flows failed with chamber pressures approaching 1 mPa. By taking great care with the insulation of all equipment attached to the target chamber, it was possible to minimise leakage currents and obtain satisfactory current integration for beams of 20 nA and above.

X-ray background problems arising from beam halo have been overcome by using graphite screens, beam skimmers and appropriately positioned X-ray shielding.

#### 4.2 Data Acquisition Facilities (M. D. Scott, R. J. Cawley)

The PDP-15 system continues to provide reliable service (except for intermittent faults associated with the I/O processor problems noted in earlier reports) and was regularly used for extended periods of unattended experiment control and data logging. The direct access spectrum storage facility has been enlarged to accommodate over 600 x 1000 channel spectra.

The PDP-7 is becoming more unreliable each year. Faults have been experienced with the memory, power supply, paper tape reader and paper tape punch, several of which spontaneously disappeared precluding proper diagnosis.

A PDP-11/GT40 computer and display system has been connected to the site Dataway network. One graphics terminal and one alphanumeric terminal are used in data processing tasks requiring access to the IBM 360 system. Numerous data processing routines have been developed for experimental use.

A two-day workshop on Pulsed Data Acquisition was organised to summarise Lucas Heights experience on signal and data transmission storage and processing and to consider problems arising in plasma physics experiments. Representatives from four Australian universities and five divisions at Lucas Heights participated in the

workshop and agreed to continue further discussions on these topics.

A magnetic tape datalogger was modified to read back field recorded tape in conjunction with an amplifier module constructed by Instrumentation and Control Division. The signals were interfaced to the PDP-15 via a Borer CAMAC module. A special handler routine was incorporated in the program PHAFSCL, which provided a useful general I/O path for block data from any CAMAC module. Difficulties were encountered with shielding the tape head and input leads from electrical interference some of which surprisingly were traced to stray 50 Hz magnetic flux in many\* NIM bins. Data can now be read with good reliability, providing the tape drive is manually controlled.

#### 4.2.1 Bibliography (J. R. Bird, B. L. Campbell<sup>\*</sup>, R. J. Cawley)

The computerised file of references on prompt nuclear analysis has now been published as an AAEC report<sup>†</sup> which includes indexes to references relating to ion backscattering, ion induced reactions, neutron induced reactions and photon induced nuclear reactions. The file and sort routines (BIBLIO) have been found to be very useful for indexing small collections of papers on other topics as a supplement to the more general profiling systems which are widely used. An advantage of BIBLIO is the flexibility that it provides in the selection of characters which can be used for search operations.

### 4.3 Ion Scattering and Implantation

#### 4.3.1 Ion scattering techniques (M. D. Scott)

A prototype permanent magnet separator was developed and evaluated for protecting surface barrier detectors from an excessive flux of low energy scattered beam particles. The separator was shown to be useful for detecting surface traces of heavy elements by proton backscattering and measuring oxygen concentration by the  $^{18}\text{O}(\text{p},\alpha)$  reaction. The technique is of little use for  $\alpha$ -particle backscattering due to the mixture of charge states of emerging  $\alpha$ -particles. A new magnet configuration has been designed to increase the collection efficiency for reaction product ions.

Two series of samples, each representing successive stages in the plating of chrome black layers on a nickel plated mild steel backing were studied using backscattering of  $\alpha$ -particles at 2.5 MeV and  $^{18}\text{O}(\text{p},\alpha)$  reaction with protons of 0.84 MeV. The backscattering results are consistent with the conventional peeling-replating model of chrome black deposition.

Fortran programs were written to supply calibration data for backscattering spectra and interactive computer simulation of such spectra is being developed for interpreting experimental backscattering results from targets having thin surface layers.

#### 4.3.2 H and He implantation (M. D. Scott)

Protons and alphas were implanted into Si wafers for Professor D. Beanland (Royal Melbourne Institute of Technology) to allow assessment of the implant zone as an infrared waveguide. Ion energies of 0.75 and 1.00 MeV were used with doses

---

\*Isotopes Division  
<sup>†</sup>AAEC/E443



up to  $5 \times 10^7$  ions  $\text{cm}^{-2}$ . The targets were moved past a stationary 1.5 mm diameter beam at currents of approximately 1  $\mu\text{A}$ . At very slow scan rates it was found that 2 mA of alphas was sufficient to melt the silicon surface. Stepping pulses to drive the sample mover were derived by prescaling the beam current integrator output pulses by a factor appropriate to the required dose rate.

#### 4.4 Proton Decoration of Fluorite (J. R. Bird, R. W. T. Wilkins\*)

In a collaborative project with CSIRO Division of Mineral Physics, an unexpected discovery was that proton irradiation of natural fluorite crystals produces decoration, colouration which reveals striking details of growth and deformation features within the crystals (Figure 4.1).

Irradiation of fluorite crystals by  $\gamma$ -rays or electrons produced a characteristic purple-pink colouration and a similar effect was observed for proton or alpha-particle irradiation of synthetic crystals. However, a few minutes irradiation with 2.5 MeV ions produces decoration which can then be studied at any later time using an optical microscope.

Measurements of the absorption spectra of irradiated spots in several samples, including synthetic fluorite, showed an expected dominant band in the 580 nm region. However, the absorption spectra from different samples was far from identical. Likewise, proton induced X-ray spectra also varied from sample to sample, but these were subject to a high background caused by the  $\gamma$ -rays produced by nuclear reactions in fluorine. Further information is needed to explain the detailed mechanism of the decoration process.

The decoration patterns showed the presence of growth features such as banding, dislocations and lineage boundaries and of deformation band boundaries, kink bands and healed fracture surfaces. Some irrelevant features, such as surface scratches also coloured. The patterns of decorated features that were found in association with fluid inclusions made it possible to clearly distinguish those formed at the time of growth from those formed during the healing of cracks. Proton decoration is thus a very simple and useful technique for studying conditions associated with the growth of natural crystals and associated mineral occurrences.

#### 4.5 Proton Induced X-rays (D. Cohen, P. Duerden, E. Clayton)

Two possible methods are being tested for the automated analysis of proton induced X-ray spectra. The first is on-line analysis and the second is batch processing in which many spectra taken under standard conditions are fitted by calculated curves which can then be examined and, if necessary, reanalysed in greater detail.

For thick targets, as used in this work, the basic X-ray emission theory must be modified to allow for the effects of proton slowing down in the sample and the attenuation of the resultant X-rays. Calculations of X-ray yield were made for ore samples used in Th/U analysis. These gave good agreement with experimentally measured yields, as shown in Table 4.2.

---

\* CSIRO Mineral Research Laboratories

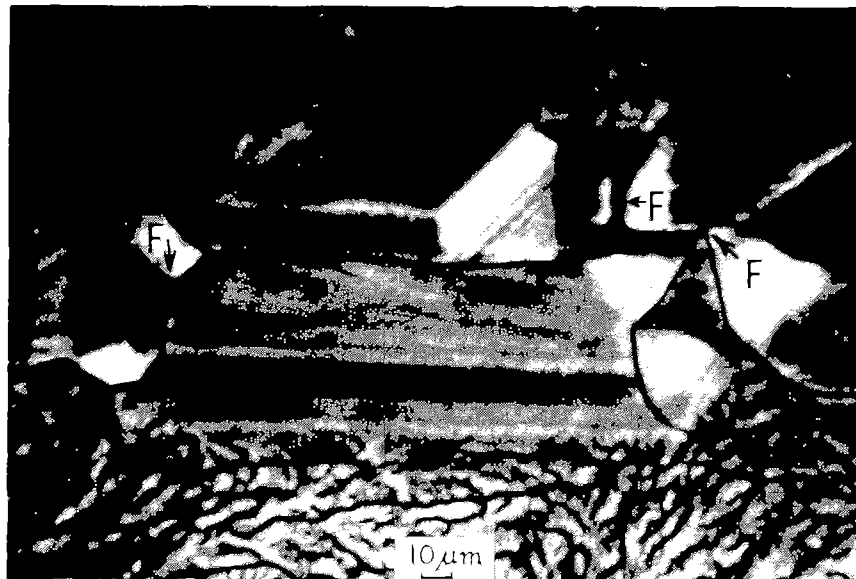


Figure 4.1

Proton irradiation of fluorite crystals induces colouration which reveals structural features such as fluid inclusions (F), healed fracture surfaces and growth dislocations.

TABLE 4.2  
COMPARISON OF THEORETICAL AND EXPERIMENTAL L $\alpha$  X-RAY YIELDS

Matrix	L $\alpha$ counts/100 $\mu\text{g g}^{-1}$ /100 $\mu\text{C}^*$			
	Calculated		Experimental	
	Th	U	Th	U
Carbon	280 $\pm$ 25	263 $\pm$ 24	296 $\pm$ 20	258 $\pm$ 20
Ore SY2E	320 $\pm$ 32	302 $\pm$ 30	328 $\pm$ 30	284 $\pm$ 25
Ore GSP1	320 $\pm$ 32	302 $\pm$ 30		

\*For  $E_p = 2.26 \text{ MeV}$ ,  $\Omega = 2.2 \times 10^{-3} \text{ sr}$  for a carbon and ore matrix using 4 layers of Perspex filters

Proton induced X-ray measurements were used in a number of exploratory experiments aimed at establishing the scope of the technique. Samples included soils, wheat, teeth, ochres, glass and artifacts such as ancient bronze or obsidian. The methods of measurement and analysis were prepared for publication.

The PIXE technique was found to be very successful in showing the changes in composition from one source of volcanic obsidian to another. Information on at least 12 elements can be extracted by simple analysis of spectra obtained in 5 to 10 minutes measuring time and a further 5 or more elements can be determined by spectrum fitting techniques. Studies of obsidian from the south-west Pacific region showed major changes in composition from one source to the next and a high degree of correlation between results for samples from the same source. Similar measurements were made on a number of tektites.

In collaboration with Dr. A. Chaudhri (Flinders University), measurements were made of proton induced X-rays from healthy and diseased teeth. Minor and trace element compositions were found to differ greatly in the two types of sample and variations throughout one tooth can also be studied.

Uranium and thorium content of clays were determined at levels of  $10 \mu\text{g g}^{-1}$  and above (in collaboration with Professor J. Prescott, University of Adelaide). Although this method may be useful in conjunction with thermoluminescent methods for dating clay products, limits are imposed on the sensitivity achieved by interference from Rb and Sr K X-rays with the L X-rays from U and Th.

#### 4.5.1 Thorium and uranium analysis (P. Duerden, D. D. Cohen, E. Clayton)

The success of the AAEC uranium analysis service brought several enquiries about the possibility of a similar service for thorium ores. Several possibilities were investigated and are currently the subject of an intercomparison. One method, proton induced X-ray emission (PIXE) offers prospects for uranium and thorium analysis simultaneously.

Ore samples, prepared by pressing the supplied powders into 12.7 mm diameter SPEX caps, are irradiated with 2.3 MeV protons from the 3 MeV Van de Graaff accelerator and the characteristic X-rays (10-19 keV range) are detected by an

intrinsic silicon detector (FWHM 310 eV at 13 keV). This energy range includes characteristic L X-rays from Pb, Th and U, as well as K X-rays from As, Se, Rb, Sr, Y and Zr. The number of counts in the K $\alpha$  or L $\alpha$  X-ray peaks of each element is obtained from fitting routines. A typical ore spectrum and its analysis is shown in Figure 4.2.

The technique has been verified by irradiating standard targets of known concentrations of Th and/or U in graphite and targets of ores and powdered rock samples whose bulk and trace concentrates has been previously measured by other methods. The Th/U experimental peak areas are plotted against concentrates in Figures 4.3 and 4.4. Good linearity over four decades of concentrates 1-1000  $\mu\text{g g}^{-1}$  was obtained for both the Th and U results. The standards (X) and ores (O), together with their least squared fitted lines, are shown separately on each graph.

X-ray yields in thick targets, which took into account the proton energy loss due to collisions with matrix atoms and the attenuation of X-rays within the matrix, have been calculated for the graphite standards and for both a granite and syenite ore. The experimental yields are in excellent agreement with the calculated thick target yields for both carbon and ore matrices. The thick target calculations indicate that any variation in yield because of ore composition is within the accuracy of the experiment.

In the present system for a 100  $\mu\text{C}$  run (5 min at 350  $\mu\text{A}$ ), the minimum detectable concentration for Th and U is 3-4  $\mu\text{g g}^{-1}$  with 25% precision for concentrations <100  $\mu\text{g g}^{-1}$  and 10% precision for concentrations >100  $\mu\text{g g}^{-1}$ . Thorium concentration cannot be measured if the Rb concentration in the sample is greater than 40 times the Th concentration or the U concentration is greater than 90 times the Th concentration. An increase in energy of the incident protons and some minor physical changes to the system should enable the minimum concentration detectable to be lowered to  $\sim 2\text{-}3 \mu\text{g g}^{-1}$ . Installation of a new detector (FWHM  $\sim 180$  eV) will reduce the interference from adjacent elements.

#### 4.6 Moata Applications (T. Wall, D. Wilson)

##### 4.6.1 Uranium analysis

The uranium analysis service continued to function smoothly. In the 12 month period, October 1, 1977 to September 30, 1978, 10 017 separate samples were analysed of which 7680 were from outside organisations and 2337 were internal AAEC requests.

The analysis of uranium in soils was extended to samples taken by the New Zealand Fertiliser Manufacturers Research Association and a similar result, that uranium deposited by superphosphate application remains undisturbed in the soil, was obtained to that of previously reported analyses of United Kingdom soils. These results have been combined in a single paper submitted to the Journal of Soil Science.

##### 4.6.2 Neutron radiography

The La Trobe University's School of Agriculture's project involving the neutron radiography of plant roots continued with the study of root behaviour

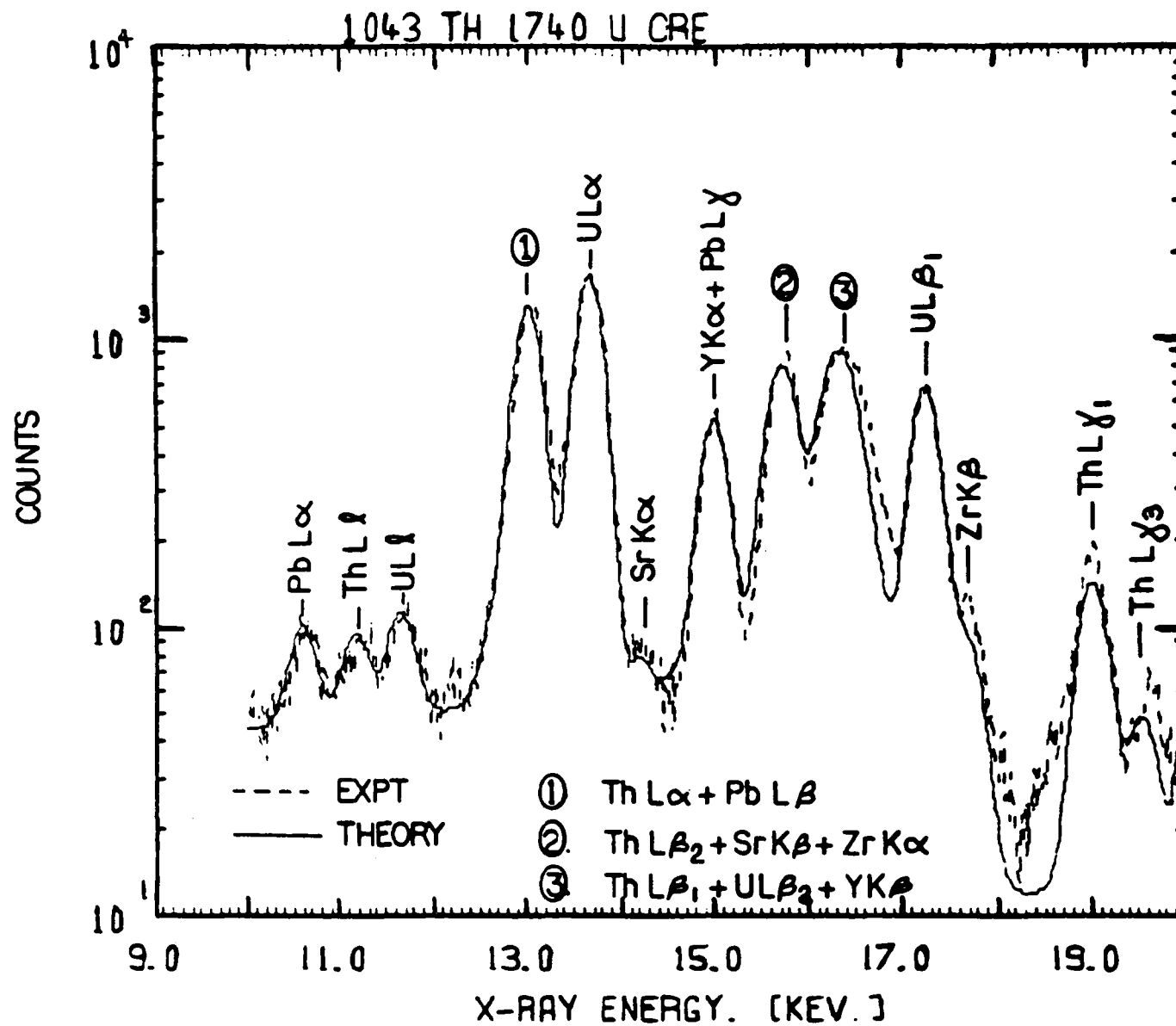


Figure 4.2 Typical PIXE spectra

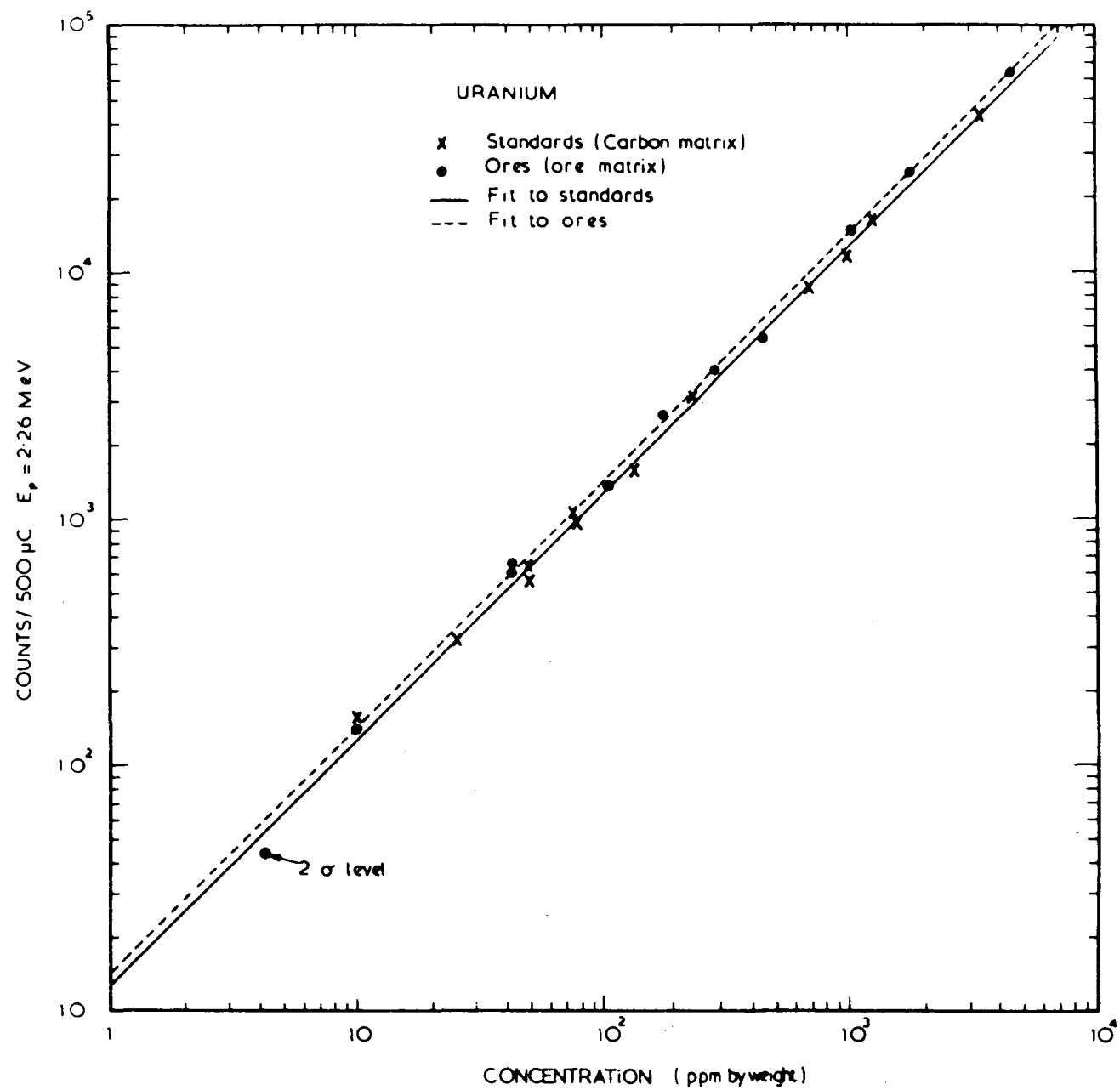


Figure 4.3 Uranium concentration as a function of induced X-ray activity

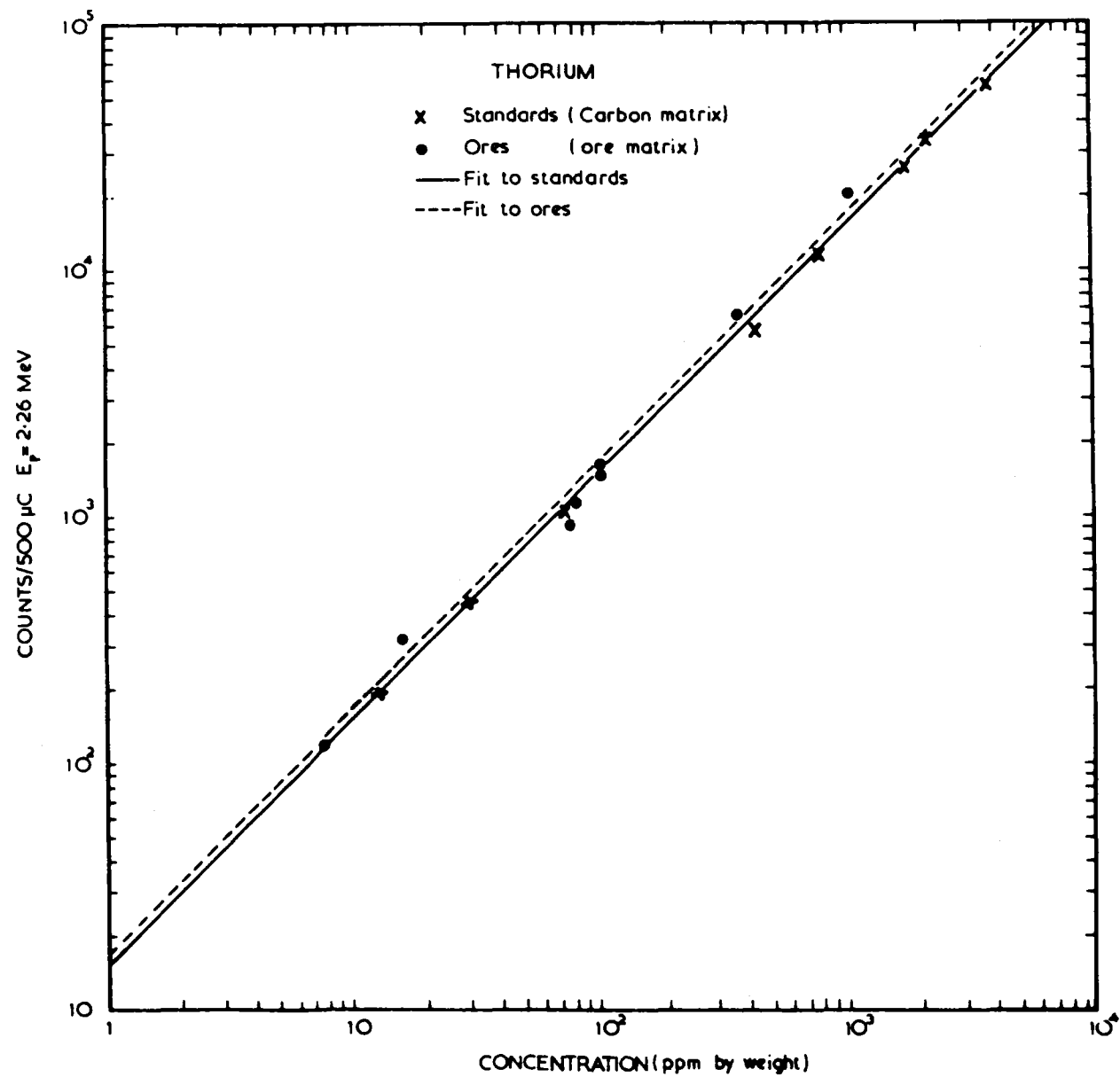


Figure 4.4 Thorium concentration as a function of induced X-ray activity

through compacted soil layers of differing density. Results indicated that some plant species can develop a root system which approaches a dense soil layer at oblique angles to aid penetration across the layer surface.

Routine neutron radiography of Boeing 747 door thrusters continued on a commercial basis.

#### 4.6.3 Thorium analysis

A preliminary analysis of ore samples and geochemical standards by neutron activation analysis using Moata showed good agreement of Th and U values with those previously obtained by PIXE analysis on the same samples. Using the delayed neutron analysis rig, each sample was irradiated for 3 min and analysed for U and then, after a 4 week cooling period, analysed for Th by gamma spectrometry. This procedure was only suitable for samples containing more than  $100 \mu\text{g g}^{-1}$  Th. The 7 hour irradiation of 40 samples irradiated together in the internal reflector stringer facility of Moata will provide analysis results down to  $1 \mu\text{g g}^{-1}$  Th.

#### 4.6.4 Particle track analysis

The presence of fissionable material in sand samples was detected by irradiating cascade impactor samples in contact with mica SSTRs.

#### 4.7 Bore Hole Logging (B. McGregor)

Bore hole probes measure the thermal and epithermal neutron flux and a characteristic  $\gamma$ -ray flux. In a typical setup, a  $^{252}\text{Cf}$  source is separated from the neutron and  $\gamma$ -ray detector by a 200 mm long bismuth  $\gamma$ -ray shield. The ratio of the characteristic  $\gamma$ -ray to the thermal neutron flux is approximately proportional to the grade of ore, while the epithermal to thermal flux ratio is sensitive to the usually unknown water content of the ore. Simple analyses of bore hole measurements ignore the effects of the bore hole and shield and assume a homogeneous situation. The relation between ore grade and fluxes will, however, depend on the diameter of the hole, the shield length and whether the hole is empty or filled with water.

To examine these variations from the homogeneous situation, a series of experiments is to be carried out at CSIRO, Port Melbourne. The effects of the neutron and  $\gamma$ -ray fluxes of different sized holes through a cylinder of sand with various water contents will be examined.

To provide design information for the experiments, a theoretical study was made of the effects of two hole sizes and various water contents. A first series of calculations found neutron fluxes at the detector position for empty and water filled holes. Both Monte Carlo and two-dimensional transport codes were used and the results compared. With the hole empty, the two methods were in good agreement. For a 12.7 cm diameter hole, the effect of the hole was to increase the neutron flux at all energies compared to the homogeneous case. For a larger hole, the fast and epithermal fluxes increase, but the thermal flux decreases. A second series of calculations compared important flux ratios in the empty holes to those at corresponding points inside the sand and to the homogeneous case for three water contents of sand covering the range of water found in most host rocks.



## 5. RUM JUNGLE ENVIRONMENTAL STUDIES (I. Ritchie, J. Harries, J. Daniel, B. Clancy)

### 5.1 Determination of Ground Water in White's Overburden Dump

A method of calibrating neutron moisture meter probes in the laboratory is to measure the count rate from the instrument when it is immersed in a well-defined mixture of dry sand and a hydrogenous material such as sugar or polythene beads to represent water. A 44 gallon drum is commonly used as a container for such calibrations. Multigroup transport theory calculations have shown that for a range of "water" contents that span part of the range of interest in field studies, the neutron leakage rate from an assembly the size of a 44 gallon drum is high and too high to make this calibration technique reliable for measuring events where the neutron moisture meter is used in an effective infinite medium.

Comparison of measurements in such assemblies, containing mixtures of sand and polythene beads in varying ratios, with the results of a multigroup transport theory calculation showed good agreement, within the accuracy of the measurement, with the count rate increasing with increasing "water" density. However, count rates measured along the axis, close to the centre of the drum, vary in a manner different to that expected from the geometry of the system and differently from mixture to mixture. The variation was at most 2.5% (see Figure 5.1) and suggested inhomogeneities in the density of the mixture.

Because of the problems of achieving mixtures of well-defined density and "water" content and the problems of relating the measurement to field results, it was decided to use calculations to provide a calibration curve and carry out a few spot checks using laboratory measurements in assemblies with high hydrogen content and hence low leakage. A two-dimensional multigroup diffusion theory code was used as the calculational tool to describe the source, counter and counter shield system of the neutron moisture meter used. However, the large thermal neutron absorption of the Pu-Be neutron source and the lithium glass detector was a severe test of a diffusion code and further check calculations will be done using a Monte Carlo code to account for the detailed geometry of the system. The diffusion code will be used to predict the systematic trend of matrix density, water density and thermal neutron absorption cross section changes.

### 5.2 Temperature Profiles within White's Dump

Analyses of the temperature distributions down the six probe holes in White's overburden dump measured during the period September 1976 to April 1977 have yielded a number of interesting, if at times puzzling results.

In one of these holes (hole A) the temperature averaged over the length of the probe hole (18 m) varied from a high of 50.95°C in February 1977 to a low of 48°C in the following March, with a maximum recorded temperature of 58.6°C at a point some 15 m from the surface. This is well above the temperature (45°C) above which the bacteria generally believed to catalyse pyritic oxidation cease to operate. The temperature down this particular hole averages 49.53°C over the period September 1976 to April 1977. Similarly averaged temperatures in the other holes ranged from 33°C to 35.63°C. The mean monthly shade temperatures averaged over the same period was typically 28.64°C in that region.

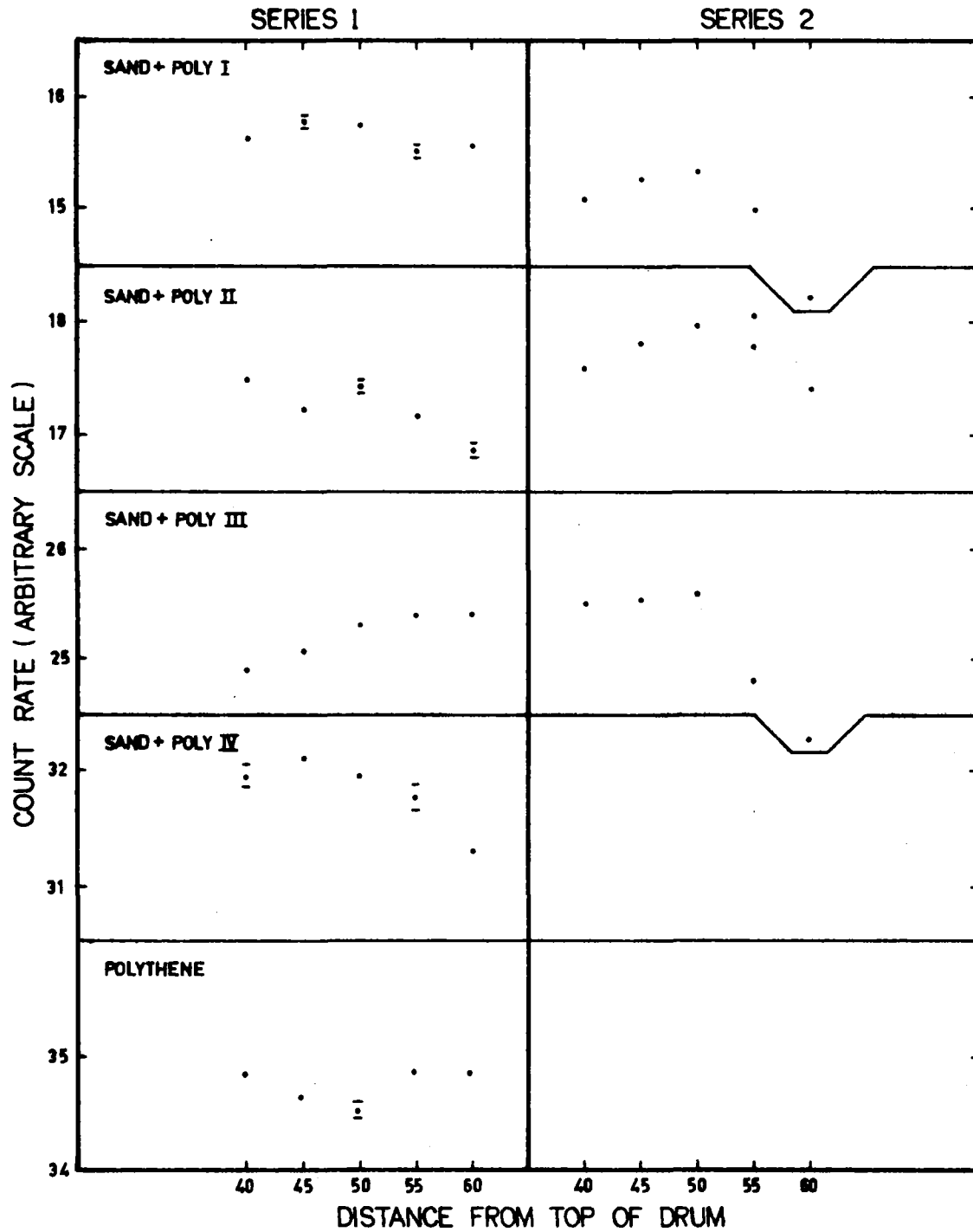


FIG: 5-1 VARIATION OF COUNT RATE ABOUT CENTRE LINE OF DRUMS FILLED WITH SAND/ POLYTHENE MIXTURES

The variation of the average temperatures about their means for the period September to April is shown for each of the holes in Figure 5.2. It can be seen that the variation of holes D, C, E and F follow a similar pattern and that the temperature in all of the holes decreases markedly in the period January to March and shows a recovery in the period March to April. As some 106.49 cm of rain fell between the observations made in January and March, while only 2.36 cm fell between the observations made in March and those in April, it would be reasonable to ascribe the temperature decreases to heat removal by water flow. However, the smallest change in the average temperature (2.06 C for hole C) from January to March, would imply a temperature change in the water running through the heap of some 18°C and an incident rain temperature of some 17°C. The largest temperature change in any of the holes in the same period would imply an incident rain temperature close to freezing. A more rigorous approach which attempted to extract the heat source distribution from the temperature profiles measured at various times, taking into account heat loss by conduction and by water transport, also led to the conclusion that some further heat removal mechanism was at work.

### 5.3 Computer Simulation of Water Flows (B. Clancy)

The computer code used to solve the water transport equations in unsaturated media was described in earlier progress reports (PR40, 41, 42). The performance of this code in simulating laboratory-scale experiments on water infiltration into rather dry soil columns was unsatisfactory in many respects and the code was completely rewritten. The major revision in the numerical analysis was the use of a complete semi-implicit scheme for the time differencing and to iterate as often as required, until the water potentials found at the end of a time step were in agreement with those used to predict the soil hydraulic properties which should apply at the end of the time step. These hydraulic properties for the end of the time step are recalculated on each iteration. Although substantially more calculation is required to complete a time step calculation successfully, larger time steps can be handled and running times for the code are considerably reduced.

When revising the code, the opportunity was taken to implement the use of SI units throughout. The revised code now simulates the laboratory scale infiltration experiments with reasonable success.

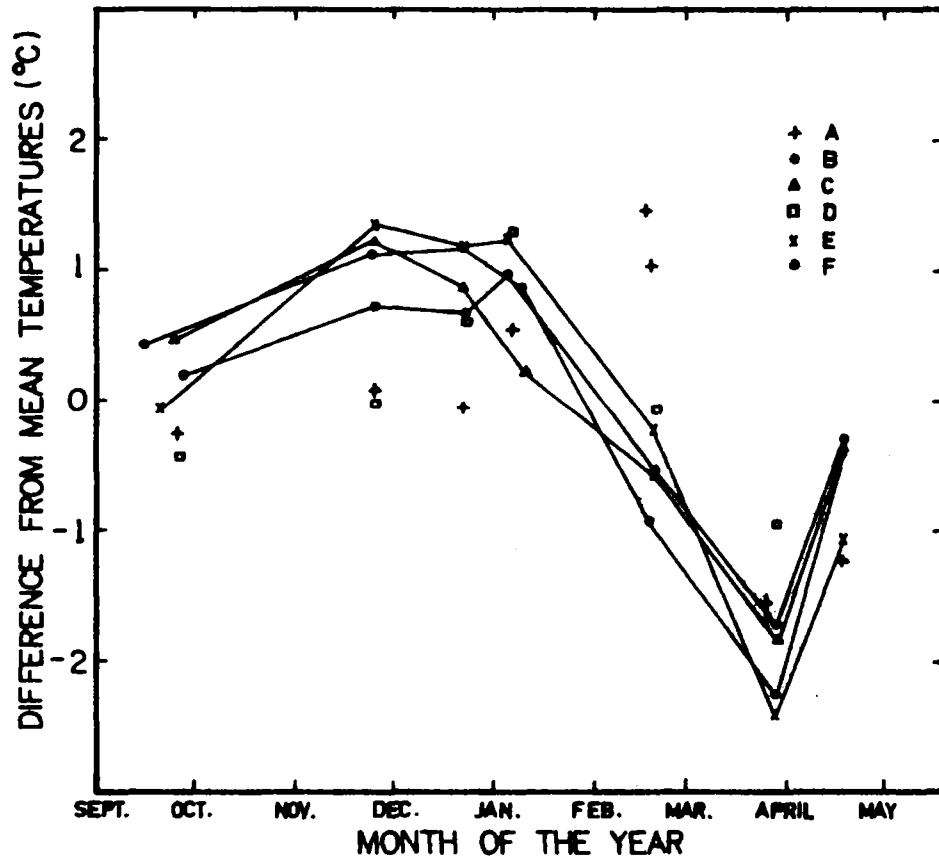


FIG: 5-2 VARIATION ABOUT MEAN OF TEMPERATURES  
WITHIN WHITE'S OVERBURDEN DUMP

## 6. FUSION

Several members of Physics Division were seconded to the three universities involved in fusion work.

### 6.1 Australian National University (G. Hogg and W. Bertram)

A small tokamak, LT-4, was constructed at the Plasma Research Laboratory, Research School of Physical Sciences, Australian National University. The basic parameters are as follows:

Plasma major radius	0.50 m
Plasma minor radius	0.14 m
Maximum toroidal field	3.0 T
Maximum plasma current	100 kA

The toroidal field coils are powered by the homopolar generator which permits plasma lifetimes of  $\sim 100$  ms, a definite advantage for diagnostic measurements.

The machine has been operated with toroidal fields of 1T, but the presence of strong magnetic fields generated by the iron core of the transformer and the toroidal field coils has limited plasma lifetime to  $\sim 10$  ms. Modifications to both the core and the field coils have been undertaken and machine operation will be recommenced shortly.

#### 6.1.1 Soft X-ray measurements on LT-4

The continuum radiation from a hot plasma reflects the distribution of electron energies within the plasma. Measurement of the X-ray (bremsstrahlung) emission spectrum permits the determination of the mean plasma electron temperature and also some knowledge of the plasma impurity content can be inferred. The overall X-ray emission intensity shows fluctuations which result from variations in electron density and temperature and which were identified as internal disruptions associated with magnetohydrodynamic instabilities.

For experiments on the LT-4 tokamak, a Ge(Li) detector\* and pulse height analysis system will be used to measure the bremsstrahlung spectrum in the range 1-30 keV, with an energy resolution of 0.2 keV at a count rate of 30 kHz. The vacuum system and detector screening are at present being assembled on LT-4.

The X-ray emission intensity will be determined by an array of silicon surface barrier detectors which view several different chords across the plasma. The detectors are sensitive to photons in the energy range 1-20 keV and each is connected to an amplifier/oscilloscope channel having a bandwidth of  $\sim 1$  MHz. An analysis system for the data is being developed.

### 6.2 Flinders University of South Australia (J. Tendys and G. Durance)

In recent years there has been a general resurgence of interest in diffuse-pinch, particularly in the reversed field pinch configuration. Since a reversed field Z-pinch reactor (RFZPR) would operate well above the Kruskal-Shafranov limit,

---

\*The detector and preamplifier were manufactured by Instrumentation and Control Division, Lucas Heights.

the tokamak related constraints of low aspect ratio, low beta value and small ratios of poloidal-to-toroidal magnetic fields no longer apply. Such a reactor would be conservative of magnetic energy and, for comparable toroidal fields, could provide larger ohmic heating rates at higher plasma densities than magnetohydrodynamic constraints allow for tokamaks. The RFZPR thus promises to be a serious contender for the role of a fusion reactor.

The linear diffuse pinch program at Flinders University is oriented towards providing information relevant to the reversed field pinch concept. The possibility of generating the required field configuration by means of a transverse rotating magnetic field is currently under investigation in FUZA-3, and the preliminary results appear very encouraging.

In addition, a systematic study of conventional "stabilised" Z-pinch is underway and this should also be of interest to people attempting to establish the reversed field pinch configuration. Preliminary studies have been completed on a small linear pinch (FUZA-1) which employed a novel capacitive-inductive storage circuit to produce the desired fast rising current and to inhibit secondary breakdown. This work is now continuing on a longer Z-pinch device (FUZA-2) which, compared with FUZA-1, has better preionisation, improved vacuum technology and larger current with increased rate of rise. The initial phase of the FUZA-2 studies concentrated on the effects of preionisation on the pinch and instability characteristics.

Wave propagation studies have also been of continuing interest and are being performed in the plasma source FPS-2. In particular, the use of magnetoacoustic oscillations as a diagnostic technique is being developed. This work will be extended to include current-carrying plasmas.

Plans are also underway to equip the plasma laboratories with computer-based data acquisition systems.

G. Durance assisted with the FUZA-2 measurements and this provided a good insight into experimental fusion studies and enabled considerable experience to be gained in a relatively short time on the operation of the machine and in the use of certain diagnostic techniques including voltage and current measurements, magnetic probe measurements, streak and framing photography and holographic interferometry. He is also playing a role in implementing the data acquisition systems.

J. Tendys did stability analysis calculations relevant to the linear diffuse pinches. He implemented on the Flinders University computer system an ideal magnetohydrodynamic code, THALIA, written at the Centre de Recherche en Physique des Plasmas, Lausanne, Switzerland. The results obtained from these calculations were compared with another stability code existing at Flinders. The two codes agreed reasonably well, using the magnetic field profiles from FUZA-1. A detailed analysis of the spectrum will be made when FUZA-2 results are available. Work is also starting on a dissipative magnetohydrodynamic code in conjunction with a university staff member.

### 6.3 Sydney University (I. J. Donnelly)

#### 6.3.1 Plasma heating due to magnetic field reversal

The SUPER-VI device at the Department of Plasma Physics, Sydney University, is a 1.7 m long coaxial shock tube of inner radius 5 cm and outer radius 11 cm filled with hydrogen at 6.6 Pa. In one series of experiments, an initial azimuthal field is set up, a plasma established and a voltage applied between the inner and outer electrodes. A current flows down the inner electrode, then in a radial sheet through the plasma and returns via the outer electrode. The radial current sheet forms a magnetic piston which moves down the tube, generating a magnetohydrodynamic shock wave in the plasma in front of it. Typical speeds are  $1.6 \times 10^5 \text{ ms}^{-1}$  for the shock wave and  $1.3 \times 10^5 \text{ ms}^{-1}$  for the piston. If the current flow is chosen so as to reverse the direction of the initial azimuthal magnetic field, then there is a point in the piston at which the field is zero, resulting in compression and heating of the plasma. Preliminary analysis of the compressive and ohmic heating of the electron gas at the field reversal point predicts electron temperatures considerably less than those found experimentally. A numerical analysis of the electron temperature and density near the piston is being attempted. If, as expected, the calculated temperature is too low, then this would indicate the presence of an anomalous resistivity which could be due to a tearing mode instability in the piston.

#### 6.3.2 Tearing mode instabilities

Internal disruptions observed in recent tokamak experiments are probably due to tearing modes, resistive magnetohydrodynamic instabilities which manifest themselves in the filamentation of current sheets. A study of the growth rate and non-linear behaviour of the tearing mode in a partially ionised plasma is being made to assess the effect of neutrals on the behaviour of this instability. It is known from linear analysis that the neutrals effectively increase the plasma density for small perturbations; however, as the mode grows it is possible that the extra dissipation due to ion-neutral friction will be important. This study is primarily of importance for astrophysical applications. The importance of the tearing mode in the reversed field pinch experiment is also being studied.

### 6.4 Plasma Equilibrium Calculations (B. Clancy, J. L. Cook)

Work has begun on the calculation of number density balance in the corona model of a plasma with diffusion in space included for a cylindrical plasma column. For the five main processes in a clean plasma rate coefficients have been evaluated, except for the emission rates of line radiation which may be included by theoretical calculations. The diffusion coefficients for elastic electron-electron, electron-ion, and ion-ion collisions have been calculated from the Born approximation, but the neutral ion diffusion poses some problems, as inelastic processes dominate.

The aim is to prepare a code which ultimately will include impurity ions as the data becomes available. Some information exists for helium oxygen and iron in the form of cross sections for ionisation and neutralisation, but these have not yet been converted to the rate coefficients. It is assumed that the temperature profile is known and it is proposed to determine the density of each of the ion species as a function of the minor radius. Other quantities which can be found are the effective

Z of all the plasma, the radiated power loss and the extent to which the plasma may depart from ionisation balance.

#### 6.4.1 Fusion data library (J. L. Cook, E. K. Rose)

The most important quantities to be calculated for the number density balance in a clean D-T plasma are the reaction rate coefficients for the various processes. The most important of these are ionisation by electron impact, auto-ionisation, dielectronic recombination, radiative recombination and ionisation by ionic impact. Altogether, we found information in the literature for 25 cross sections and theoretical calculations can supply the missing information. A program was written which averages the cross sections times the species velocity over a Maxwellian spectrum. These evaluations are almost complete.

#### 6.4.2 Atomic and molecular data needs for fusion reactors (M. J. Kenny)

The current research activity aimed at producing controlled thermonuclear reactors has led to a list of data needs and priorities concerning atomic and molecular interactions within the plasma and with the wall materials. The number of possible interactions is quite large and, in most cases, reaction rates for such processes as charge exchange, ionisation, dissociation and recombination, are not known to the required degree of accuracy. Recently, the IAEA became involved in the collection and dissemination of data and requests.

A survey was carried out within Physics Division of some of these needs. The survey was confined to the field of charged particle reactions with ion energies in the range from several hundred keV to 3 MeV. It aims at identifying areas of greatest need for charged particle reaction information. Such areas include plasma diagnostics, interaction of helium ions with wall materials, impurity effects and plasma energy losses.

The survey concluded that a considerable amount of research is required in atomic and molecular interactions in the short to medium term future if the CTR program is to reach the situation of economic power generation.

### 7. MISCELLANEOUS

#### 7.1 Magnetohydrodynamic Turbine (D. W. Lang, J. P. Sawyer)

A model to demonstrate the feasibility of the device is in the process of construction. Design has been completed and components and materials are being collected. The major machining tasks have been started. It is intended to use the model first for a qualitative demonstration and afterwards to check the performance as some of the parameters are varied.

#### 7.2 Application of Unfolding Techniques

##### 7.2.1 Measured resolution functions (D. Lang)

It was reported earlier (see AAEC/PR40-P, section 4.4, AAEC/PR43-PH, section 4.4.4) that a program was written to unfold the effects of resolution functions that were measured rather than calculated.

The data to be unfolded has sufficient statistical accuracy to allow considerable investigation of details of the unfolding process. The most important



consideration in any fitting routine with least squares is a product matrix  $R^T \omega^2 R$  generated from the resolution function matrix,  $R$ , its transpose and a diagonal weight matrix. In general terms, the closer the matrix is to the diagonal form, the easier the fitting process becomes.

It was found that the resolution functions associated with detection of neutrons in a scintillator did not lead to a specially convenient matrix. There were however, fewer problems than expected with the effects of measured resolution functions. The unsmoothed functions were nearly as efficient as the smoothed ones in unfolding and appeared to give no systematic errors.

Considerable success has been obtained with a modified conjugate gradient technique which first unfolds the information associated with large eigenvalues of the product matrix and afterwards various selections of the medium sized eigenvalues.

#### 7.2.2 Activation methods to determine neutron flux

The major limitation in any unfolding program is the structure of the resolution matrix,  $R^T \omega^2 R$ . All information about the unfolded flux can be expressed as a linear combination of the resolution functions. The forms of activation cross sections are badly matched to the sort of neutron fluxes that occur. Perhaps the most serious region of disagreement is that for a thermal neutron flux, which must be close to Maxwellian in form and for which the activation cross sections are either below threshold and hence zero, or in a  $1/v$  region.

It has been noted that the neutron flux is needed, not usually on its own account, but as a step in evaluating some other quantity such as damage to a crystalline material. A program is being written to evaluate upper and lower limits of the damage, given a cross section for damage as a function of energy of the neutron flux, and subject to linear programming constraints on the activation integral and for positive neutron flux.

#### 7.2.3 Flux spectrum unfolding for HIFAR (J. L. Cook, H. D. Ferguson)

An interactive program was written which solved the activation rate equations obtained by Isotopes Division for 14 reactions in activation detectors placed in various regions of HIFAR. The equations were to be solved using a special constrained linear least squares method developed by us and which gave good results for test problems. A 100 group energy-dependent flux was to be evaluated in 5 rig positions. The appropriate cross section data library was prepared, but although the experimental data is now available, the project has been put in abeyance through lack of effort.

#### 7.3 Neutron Therapy (B. McGregor)

The changes in the shape of different accelerator produced neutron spectra were calculated as the neutrons travelled through a phantom representing the human body. Calculations were made with one- and two-dimensional SN (DOT) and Monte Carlo (MORSE) codes. The DOT calculations required the first collision source method to remove ray effects. Agreement was obtained between MORSE and DOT in the calculated spectra at various depths. However, the spectra are higher in the energy range 1-4 MeV than measured at the Hammersmith Hospital Cyclotron\* unit. The reasons for this are

---

\*Hammersmith Hospital, London

under investigation.

During the course of this study, errors were found in the cross section preparation codes APRFX and ANISN.

#### 7.4 Deep Ocean Currents and Disposal of Radioactive Waste into the Ocean

(J. R. Harries)

A review of the physical properties of the deep ocean that are relevant to ocean disposal of radioactive waste is being prepared. The review is concentrating on the properties of the Pacific and Indian Oceans to provide a basis of estimating the transport of materials towards Australian waters. The complexity of the physical circulation and chemical transport paths are in marked contrast to the simplified models which have been developed to determine the limits to radioactive dumping.

To gain a better understanding of transport processes, a study is being undertaken of the distribution of tritium in the waters off eastern Australia. Seawater samples were taken from the CSIRO's R.V. "Sprightly" and analysed by the Nuclear Hydrology Group of Isotopes Division for tritium concentration. The tritium concentration decreases from about 2 tritium units (TU) at the surface to less than 0.5 TU at 1000 m depth. At 400 m depth there is a higher concentration of tritium to the north-east of the east Australian current than to the south-west of the current.

#### 7.5 Inverse reaction problem (E. Clayton, J. L. Cook, E. K. Rose)

Using reaction matrix data obtained for the P11 state in pion-nucleon scattering, the structure of the meson probability density surrounding the nucleon core was calculated. The probability density exhibited nodes which separated three distinct regions which may be associated with internal particles. Calculations of the effective potential in all partial waves have been completed and show a phenomenon of singularities which move with energy from the inner regions to the surface. Whether this is related to the emission of particles such as occur in the various inelastic channels is under investigation.

#### 7.6 Pressure Dependence of Plasma Formation under Laser Radiation

(A. Rose)

Earlier experiments have shown that there is a strong relationship between breakdown and pressure in the fluoro-carbon gas analogue of uranium hexafluoride. To extend the earlier experiments, a laser (15 J lumonics TEA CO laser kit) has been purchased capable of producing higher peak powers. The basic kit is complete, except for optics and HV power supply. The user must also provide lasing gases at the correct partial pressures and flow rates.

A 40 kV, 20 mA power supply has been constructed and near totally reflecting and front partially reflecting mirrors provided to allow operation of the laser. Additional optics will be required for the breakdown measurements.

A gas supply system was built to deliver the lasing gases (carbon dioxide, helium and nitrogen) at the current partial pressures and flow rates. The complete unit has been assembled and made operational. Preliminary firings indicate that the laser will operate at the designed 15 J output at repetition rates up to 5 pulses per second.

## 8. PUBLICATIONS

### 8.1 Papers

- Allen, B. J. and Musgrove, A. R. de L. (1978) - Valence and doorway mechanisms in resonance neutron capture. *Advances in Nuclear Physics*, Vol. 10, 129. Plenum Press.
- Allen, B. J., Musgrove, A. R. de L. and Bertram, W. K. (1978) - Resonance and background interference in  $^{54}\text{Fe}$  neutron capture. *Phys. Lett.* 72B, 323.
- Barry, J. M. and Pollard, J. P. (1977) - Method of implicit non-stationary iteration for solving neutron diffusion linear equations. *Ann. Nucl. En.* 4, 485.
- Bird, J. R., Scott, M. D., Russell, L. H. and Kenny, M. J. (1978) - Analysis using ion induced  $\gamma$ -rays. *Aust. J. Phys.* 31, 209-213.
- Boldeman, J. W., Allen, B. J., Musgrove, A. R. de L. and Macklin, R. L. (1977) - The neutron capture cross section of yttrium-89. *Nucl. Sci. & Eng.* 64, 744.
- Kenny, M. J. and Allen, B. J. (1977) - Gamma rays from keV neutron capture in  $^{139}\text{La}$ . *Aust. J. Phys.* 30, 591.
- Kenny, M. J., Allen, B. J. and Macklin, R. L. (1977) - Resonance neutron capture in Sc below 100 keV. *Aust. J. Phys.* 30, 605.
- Lang, D. W. and Cook, J. L. (1978) - Phase equivalent potentials in reaction matrix theory. *Aust. J. Phys.* 31, 215-18.
- Musgrove, A. R. de L., Allen, B. J. and Macklin, R. L. (1977) - Resonance neutron capture in  $^{139}\text{La}$ . *Aust. J. Phys.* 30, 599.
- Musgrove, A. R. de L., Allen, B. J. and Macklin, R. L. (1978) - Neutron capture resonance parameters and cross sections for the even-A isotopes of cadmium. *J. Phys. G.* 4, 771.
- Musgrove, A. R. de L., Allen, B. J. and Macklin, R. L. (1978) - Resonance neutron capture in  $^{138}\text{Ba}$  and  $^{140}\text{Ce}$  and the prompt neutron correction to gamma ray detectors. *Aust. J. Phys.* (in press).

### American Physical Society Meetings

- Kenny, M. J., McCullagh, C. M. and Chrien, R. E. (1977) - Gamma-ray transitions in the 5.9 keV  $^{27}\text{Al}$  resonance. *Bull. Am. Phys. Soc.* 22, 995.
- Kenny, M. J., Liou, H. I., Chrien, R. E. and Stelts, M. L. (1978) - Neutron cross sections for thorium. *Bull. Am. Phys. Soc.* 23, 637.
- McCullagh, C. M., Kenny, M. J. and Chrien, R. E. (1977) - Spin determination of the 398 eV  $^{35}\text{Cl}$  resonance. *Bull. Am. Phys. Soc.* 22, 995.
- Stelts, M. L., Kenny, M. J., McCullagh, C. M., Chrien, R. E. and Goldhaber, M. (1978) - The angular distribution and branching ratios for the  $^{20}\text{B}(n,\alpha)^7\text{Li}$  reaction at 2 and 24 keV. *Bull. Am. Phys. Soc.* 23, 526.

## 8. PUBLICATIONS

### 8.2 Reports

- Bird, J. R., Campbell, B. L. and Cawley, R. J. (1978) - Prompt nuclear analysis bibliography 1976. AAEC/E443.
- Cawley, R. J. and Bird, J. R. (1978) - BIBLIO - a bibliographic index system. AAEC/E449.
- Cawley, R. J. and Trimble, G. D. (1977) - An interactive computing system for the AAEC Dataway network. AAEC/E425.
- Clancy, B. E. (1978) - COMFORT - an interactive FORTRAN system for the IBM 360 computer. AAEC/E454.
- Cohen, D. and Duerden, P. (1978) - Proton induced X-ray emission (PIXE) analysis at Lucas Heights. AAEC/E453.
- Connolly, J. W. and Ferguson, H. (1978) - An analysis of self-terminating power transients in the reactor HIFAR. AAEC/E435.
- Harries, J. R. and Wilson, D. J. (1978) - Measurement of the dynamic response of HIFAR. AAEC/E428.
- Harries, J. R. (1978) - Inverse kinetics measurements on HIFAR. AAEC/E456.
- McCulloch, D. B. and Connolly, J. W. (1977) - Measurement and calculation of slow power transients in the university training reactor, Moata. AAEC/E422.
- McCulloch, D. B. (1977) - Reactor physics activities in Australia, 1976-1977. NEACRP-L180a.
- McCulloch, D. B. (1978) - Reactor physics activities in Australia, 1977-1978. NEACRP-L202a.
- Pollard, J. P. (1978) - SKAN - a free input labelled output variable dimensioning routine for the IBM 360 computer. AAEC/E431.
- Rainbow, M. T. (1978) - Applications of the MORSE Monte Carlo transport code to the calculation of pulsed neutron experiments. AAEC/E461.

### 8.3 Conference Papers

- Boldeman, J. W. (1977) - Review of  $\bar{\nu}$  for  $^{252}\text{Cf}$  and thermal neutron fission.  
Proc. Int. Specialists' Meeting on Neutron Standards and Applications,  
Gaithersburg, p. 182.
- Cohen, D., Duerden, P. and Clayton, E. (1978) - The application of PIXE to uranium/  
thorium analysis in thick ore samples. 7th AINSE Nuclear Physics Conf.,  
Melbourne, Feb.
- Lang, D. W. (1978) - Reactor calculations and nuclear information. 7th AINSE  
Nuclear Physics Conf., Melbourne, Feb. Paper 18.
- Ritchie, A. I. M. (1978) - Impact on the environment of the mining operation at  
Rum Jungle. 3rd Ann. Conf. Aust. Rad. Protection Soc., May 24-26.

#### Fourth National Soviet Conference on Neutron Physics,

Kiev, 1977

- Allen, B. J., Musgrove, A. R. de L. and Boldeman, J. W. - Neutron capture mechanisms  
in the 3s and 3p regions. Vol. II, p. 149
- Boldeman, J. W., Grenier, G., Joly, S. and Voignier, J. - Etude de la capture  
neutronique resonnante de  $^{28}\text{Si}$  entre 0.5 et 1 MeV. Vol. II, p. 164.
- Caruana, J., Boldeman, J. W. and Walsh, R.L. - Fission fragment angular distribu-  
tions for neutron fission of  $^{232}\text{Th}$  and their interpretation with a triple-  
humped barrier. Vol. III, p. 52.
- Caruana, J., Boldeman, J. W. and Walsh, R. L. -  $\bar{\nu}_p$  for neutron fission of  $^{232}\text{Th}$   
near threshold. Vol. III, p. 44.

#### Specialist Meeting on Neutron Data of Structural Materials

for Fast Reactors, CBNM, Geel, Dec. 5-8, 1977

- Allen, B. J., Musgrove, A. R. de L. - s-wave resonance parameters in the structural  
materials.
- Allen, B. J., Musgrove, A. R. de L., Taylor, R. B. and Macklin, R. L. - Neutron  
capture cross section of  $^{57}\text{Fe}$ .
- Allen, B. J., Musgrove, A. R. de L., Macklin, R. L. and Winters, R. R. - Neutron  
sensitivity of capture  $\gamma$ -ray detectors.
- Allen, B. J., Musgrove, A. R. de L. and Bertram, W. K. - Resonance and background  
interference in  $^{54}\text{Fe}$  neutron capture.

Conference Papers (cont'd)

Second Australian Conference on Nuclear Techniques of Analysis,

Lucas Heights, May 15-17, 1978

- Clapp, R. A., Scott, M. D. and Bird, J. R. (1978) - A systematic investigation of solar collector chrome black surfaces.
- Clayton, E., Duerden, P. and Cohen, D. (1978) - Theoretical interpretation of PIXE spectra.
- Campbell, B. L. and Bird, J. R. (1978) - Recent developments in prompt nuclear analysis.
- Cohen, D., Clayton, E. and Duerden, P. (1978) - The proton induced X-ray emission technique for ore analysis.
- Duerden, P., Clayton, E. and Cohen, D. (1978) - The use of PIXE in the characterisation of thick obsidian samples.
- King, B. V., Kelly, J. C. and Bird, J. R. - Particle beam methods for protein analysis in wheat.
- McGregor, B. J., Dickson, R. L. and Clark, G. J. - Technique for correcting for overburden effects in ground level surveys of uranium orebodies.
- McGregor, B. J. and Eisler, P. (1978) - The effect of the bore hole itself on bore hole logging measurements.
- Scott, M. D. and Russell, L. H. (1978) - Magnetic separation as an adjunct to surface barrier detectors for backscattering and ion reaction analysis methods.
- Scott, M. D., Russell, L. H., Duerden, P., Cohen, D., Clayton, E. and Bird, J. R. - Studies of artifacts using ion beam techniques.
- Wall, T. - Delayed neutron analysis service work and applications.
- Wilkins, R. W. T., Bird, J. R. and Scott, M. D. (1978) - Decoration of growth and deformation dislocations in fluorite.
- Willatt, S. T., Wall, T. and Gillespie, P. - Neutron radiography of plant root growth.

International Conference on Nuclear Interactions

ANU, Canberra, Aug. 28-Sept. 1, 1978

- Allen, B. J. and Bird, J. R. - Intermediate structure studies of the giant dipole resonance near the threshold region.
- Boldeman, J. W. and Walsh, R. L. - Fission barriers for the thorium isotopes.
- Grenier, G., Joly, S., Voignier, J. and Boldeman, J. W. - Resonance neutron capture spectroscopy in  $^{28}\text{Si}$ .
- Walsh, R. L., Boldeman, J. W. and Elcombe, M. M. - Measurements of kinetic energies of  $^{239}\text{Pu}$  fission fragments in the resonance region.

Conference Papers (cont'd)Third International Symposium on Neutron Capture Gamma Ray Spectroscopy and Related Topics, Brookhaven, Sept. 18-22, 1978

- Allen, B. J. and Musgrove, A. R. de L. - Neutron capture mechanism in the 3s size resonance, I, II.
- Allen, B. J. and Musgrove, A. R. de L. - Non-statistical neutron capture mechanisms in  $^{139}\text{La}$  and  $^{141}\text{Pr}$ .
- Joly, S., Grenier, G., Voignier, J. and Boldeman, J. W. - Gamma decay of  $p_{3/2}$  neutron resonances in  $^{28}\text{Si}$ .
- Kenny, M. J., McCullagh, C. M. and Chrien, R. E. - Gamma rays from the 5.9 keV neutron resonance in  $^{27}\text{Al}$ .
- Kenny, M. J. and Chrien, R. E. - Capture of 2 and 24 keV neutrons by the zirconium isotopes.

International Conference on Neutron Physics and Nuclear Data for Reactor and Other Applied Purposes, Harwell, Sept. 25-29, 1978

- Musgrove, A. R. de L., Allen, B. J., Boldeman, J. W. and Macklin, R. L. - Recent measurements of neutron capture cross sections in the fission product mass region.
- Musgrove, A. R. de L., Allen, B. J. and Macklin, R. L. - Resonance neutron capture in  $^{23}\text{Na}$  and  $^{27}\text{Al}$  from 3 to 600 keV.
- Boldeman, J. W., Culley, D. and Cawley, R. J. - The fission neutron spectrum from the spontaneous fission of  $^{252}\text{Cf}$ .

PHYSICS DIVISION SEMINARS

The following seminars were presented during the year. Seminar convenor was B. J. Allen.

<u>Date</u>	<u>Speaker</u>	<u>Topic</u>
2/3/78	A. I. M. Ritchie, Physics Division	Rum Jungle - Environmental Impact Post Study
30/3/78	Prof. D. W. George, Chairman, AAEC	AAEC - the next 25 years
19/4/78	M. J. Kenny, Physics Division	Nuclear Research at Brookhaven
12/6/78	Prof. T. Hamada, Visiting Prof. to University of New South Wales	Stopping Power of Plasmas
21/6/78	Prof. S. C. Haydon, University of New England	Investigation of d.c., r.f. and Laser Plasmas
13/7/78	A. I. M. Ritchie, Physics Division	Electrical Breeding - an Alternative to the FBR
19/7/78	K. Okamoto, University of NSW	Comparative study of nuclear and non-nuclear energy sources
17/8/78	B. James, Sydney University	Plasma Physics and Fusion Research
24/8/78	R. Cross, Sydney University	The Sydney University Tokamak
25/8/78	J. L. Symonds, P. Essam, K. Stocks, M. Maher, Power and Energy Unit	The analysis of Australian and State Energy Systems
11/9/78	Prof. W. Greiner, University of Frankfurt am Main	Developments in Atomic and Nuclear Physics
18/9/78	B. L. Berman, University of California	A New Nuclear Determination of the Age of the Universe





DISTRIBUTION LIST - AAEC/PR44-PD

1. Chairman
2. Deputy Chairman
3. General Manager
4. Professor H. Messel
5. Sir Bernard Callinan
6. Director
7. Deputy Director, Operations
8. Deputy Director, Research
9. Chief Scientist, Power and Energy
10. Chief Scientist, Nuclear Fuel Cycle
11. Chief, Applied Mathematics and Computing Division
12. Chief, Centrifuge Enrichment Project Division
13. Chief, Chemical Technology Division
14. Chief, Engineering Research Division
15. Chief, Environmental Science Division
16. Chief, Instrumentation and Control Division
17. Chief, Isotope Division
18. Chief, Materials Division
19. Chief, Physics Division
20. Head, Regulatory and External Relations Branch
21. Secretary and Head, Administration Branch
22. Director, Public Relations
23. Director, Nuclear Plant Safety Unit
24. Controller, Site Information Services
25. Executive Officer, AINSE
26. Library, Head Office
- 27-29 Library, R.E.
30. Washington Office
- 30-31 London Office
32. Vienna Office
33. Vienna Office
34. Tokyo Office
- 35-75 W. Gemmell (for INDC and Bilateral Agreement correspondents)
- 76-106 J. R. Bird (for special distribution)
107. B. J. Allen
108. J. W. Boldeman
109. B. E. Clancy
110. J. W. Connolly
111. J. L. Cook
112. P. Duerden
113. G. Durance
114. J. Harries
115. G. Hogg
116. M. Kenny
117. D. Lang
118. D. B. McCulloch
119. B. McGregor
120. A. Musgrove
121. J. Pollard
122. M. Rainbow
123. I. Ritchie
124. J. Tendys
125. W. Turner
126. R. L. Walsh
127. D. Byers (University of Canterbury, N.Z.)
128. V. Deniz (BARC, India)
129. S. Kapoor (BARC, India).
130. G. K. Mehta (Indian Institute of Technology)
131. S. Supadi (BATAN, Bandung)
132. I. Supki (BATAN, Bandung)
133. G. Tyror (AEEW, U.K.)
134. N. Veeraraghavan (BARC, India).
135. J. Askew (AEEW, U.K.)
- 136-156 Bilateral Agreements (UKAEA 5, US Dept. of Energy 11, AECL 5) via H.O.
- 157-200 Spares